Research Square

Preprints are preliminary reports that have not undergone peer review.
They should not be considered conclusive, used to inform clinical practice,
or referenced by the media as validated information.

# A Signed-Lorentz-Force Reduced Model for Reversed Electromagnetic Forcing in Stratified Nanofluids

**Ravinder Kumar**

ravinderkhary10@gmail.com

Maharishi Markandeshwar (Deemed to be University), Mullana, Ambala, India https://orcid.org/0000-0002-0612-2936

**Research Article**

**Keywords:** Current-opposed MHD; Electroconductive Casson nanofluid; Blasius-Sakiadis comparison; Stratified boundary layers; Lorentz force reversal; Entropy generation

**Posted Date:** November 9th, 2026

**DOI:** https://doi.org/10.21203/rs.3.rs-11633120/v1

**License:** This work is licensed under a Creative Commons Attribution 4.0 International License.
Read Full License

**Additional Declarations:** The authors declare no competing interests.

# A Signed-Lorentz-Force Reduced Model for Reversed Electromagnetic Forcing in Stratified Nanofluids

Ravinder Kumar[1]

[1]Department of Mathematics, MMEC, Maharishi Markandeshwar (Deemed to be University), Mullana, India

**Abstract**

This study investigates a *signed-Lorentz-force reduced model* for magnetohydrodynamic (MHD) forcing, $\mathbf{F}_L = -s_M \sigma_f B_0^2(\mathbf{v} - \mathbf{V})$ with $s_M = \pm 1$ and $M = s_M \sigma_f B_0^2/(\rho_f a)$, applied to stratified Casson nanofluid boundary layers in Blasius-type and Sakiadis-type configurations. The case $s_M = +1$ ($M > 0$) is the conventional Lorentz-retarding force obtained from the quasi-static MHD equations, whereas $s_M = -1$ ($M < 0$) is a postulated sign-reversed force with the same relative-velocity structure; it does not follow from reversing the electric field in the full vector Ohm's law. The electrical conductivity remains positive in both cases. The governing equations, based on the Buongiorno nanofluid model with heat generation/absorption and Darcy–Forchheimer drag, are reduced by similarity transformation and solved numerically with an adaptive RK45–Newton–Raphson shooting scheme. The current-reversed regime produces distinctive flow modifications: velocity profiles exhibit reversed trends between Blasius-type and Sakiadis-type configurations, while thermal and solutal stratification ($St$, $Ss$) consistently suppress near-wall temperature and concentration. Within the parameter range studied, the displacement thickness decreases monotonically with the Casson parameter $\beta$ for Blasius-type flow (both signs of $M$) and Sakiadis-type flow with $M > 0$, confirming boundary-layer thinning. An entropy generation analysis further shows that, for the parameter ranges investigated, the current-reversed regime generates higher total entropy than the current-aligned regime in both flow configurations. These findings position current-reversed MHD as a candidate mechanism for nanofluid flow manipulation, with possible relevance to electromagnetic microreactors and stratified-flow energy systems.

**Keywords**

Current-opposed MHD; Electroconductive Casson nanofluid; Blasius-Sakiadis comparison; Stratified boundary layers; Lorentz force reversal; Entropy generation;

## 1 Introduction

The effect of current-aligned versus current-reversed electromagnetic forcing on a three-dimensional Blasius-type/Sakiadis-type nanofluid flow is investigated in the present study. Following common

usage in the stretching-sheet boundary-layer literature [25, 33, 34, 27, 28], we refer throughout to the stationary-wall configuration as "Blasius flow" and the moving-wall configuration as "Sakiadis flow" (interchangeably "Blasius-type"/"Sakiadis-type"); as shown in Section 4.2, these reduce respectively to the classical Hiemenz stagnation-point flow and the Crane stretching-sheet solution in the appropriate limits, and are distinct from the original constant-free-stream Blasius problem and the original Sakiadis problem. The problem is analyzed in two special cases of the signed-Lorentz-force reduced model defined in Section 2: $M > 0$, the conventional current-aligned Lorentz-force reference direction ($s_M = +1$), and $M < 0$, the current-reversed case ($s_M = -1$, with the fluid's electrical conductivity $\sigma_f$ retained as a positive material property throughout), for both configurations. The interaction between nanoparticles and electric fields can significantly alter boundary-layer characteristics, particularly for non-Newtonian carrier fluids [6, 7, 8], and the directional dependence of an imposed electric field – and hence of the induced current and Lorentz force – is of particular interest in electromagnetic flow control and biomedical microfluidic applications [12, 11], motivating the present comparison of current-aligned and current-reversed cases.

The moving-plate boundary layer was first analyzed by Sakiadis [1], who showed that a surface moving at constant velocity through an otherwise quiescent fluid develops a boundary layer growing in the direction of motion – a qualitatively different problem from Blasius's constant-free-stream case. Crane [2] extended this to a linearly stretching sheet with an exact closed-form solution, and subsequent work generalized it to non-Newtonian carrier fluids [3, 4] and nanofluids [15]. Blasius [16] originally treated steady flow over a stationary surface building on Prandtl's boundary-layer concept [17]; its three-dimensional extension over a stretching sheet has since been studied numerically [18] and its stability examined both experimentally and theoretically [19, 20]. Non-Newtonian fluids, unlike Newtonian fluids such as air and water, change their viscosity and flow behavior based on applied stresses or over time; examples include honey, blood, toothpaste, paints, and shampoos. The Casson fluid is a yield-stress rheological model, *not* a power-law model: it behaves as a rigid (non-flowing) solid below a critical yield stress $\tau_0$ and as a shear-thinning viscous fluid once that stress is exceeded. Its constitutive relation for the shear stress $\tau$ is

$$\tau = \left(\mu_B + \frac{\tau_0}{\sqrt{2\pi_c}}\right)\left(\frac{\partial v_i}{\partial x_j} + \frac{\partial v_j}{\partial x_i}\right), \qquad \pi_c > \pi,$$

$$\tau = \left(\mu_B + \frac{\tau_0}{\sqrt{2\pi}}\right)\left(\frac{\partial v_i}{\partial x_j} + \frac{\partial v_j}{\partial x_i}\right), \qquad \pi_c < \pi,$$

where $\mu_B$ is the plastic dynamic viscosity, $\pi = e_{ij}e_{ij}$ is the product of the strain-rate tensor with itself, and $\pi_c$ is the critical value of $\pi$ based on the non-Newtonian model. This constitutive relation, applied to the boundary-layer momentum equations, produces an effective viscosity of $\nu_f(1+1/\beta)$, where $\beta = \mu_B\sqrt{2\pi_c}/\tau_0$ is the Casson parameter used throughout this paper; $\beta \to \infty$ (vanishing yield stress) recovers the classical Newtonian fluid, while smaller $\beta$ corresponds to a larger yield-stress contribution [21].

Fluid flow in porous media is significant for applications such as geothermal energy extraction, oil recovery, and environmental science. Foundational studies on convective transport in porous media [38, 39, 40, 41] established the boundary and inertia effects central to the Darcy-Forchheimer model

used here, and subsequent work extended these foundations to MHD and stretching-flow settings [29, 35, 36, 37, 30].

This investigation examines nanofluid dynamics under a normally-oriented magnetic field [22], focusing on current-aligned and current-reversed electromagnetic forcing with the electrical conductivity $\sigma_f$ retained as a fixed positive material property in both cases. Directional electromagnetic forcing of this kind is, in principle, relevant to geophysical and astrophysical MHD, MHD flow-control devices, and electrochemical/thermal systems involving conductive nanofluids [23, 24, 26, 31, 32, 42, 43]. The case examined in detail is one in which the induced current opposes the $M > 0$ reference direction, for a Casson nanofluid boundary layer.

**Novelty and distinction from prior work.** Three-dimensional Blasius/Sakiadis flow [18, 19, 20], Casson nanofluid boundary layers [21], and Darcy-Forchheimer porous-medium MHD flow [25, 27, 33, 34, 28] have each been studied extensively, though largely in isolation from one another. Ridha [18] treated three-dimensional Blasius flow, and Pantokratoras [28] extended this to a Carreau fluid, but neither considered Casson rheology, porous drag, MHD, stratification, or entropy generation. Mustafa et al. [33] examined MHD effects on a Maxwell fluid, but only in the Sakiadis (not Blasius) configuration, without porous drag, stratification, or entropy generation. Kumar et al. [21] combined Casson/Carreau rheology with Darcy-Forchheimer porous drag and stratification, but for neither a three-dimensional Blasius/Sakiadis flow nor an MHD forcing term. Kumar et al. [25] studied three-dimensional MHD flow, and Kumar et al. [27] studied Darcy-Forchheimer porous drag, but neither paper included Casson rheology, stratification, or entropy generation, and [25] did not include porous drag while [27] did not include MHD. Xiangyang et al. [34] combined porous drag with MHD, but in a channel-flow (not boundary-layer) geometry, again without Casson rheology, stratification, or entropy generation. In every one of these studies, where MHD is considered at all, $M$ is treated as a positive Hartmann-type parameter representing the conventional current-aligned Lorentz retarding force; among the studies we have reviewed, none combines a signed/reversed-current formulation with the three-dimensional Blasius/Sakiadis comparison, Casson rheology, Darcy-Forchheimer porous drag, stratification, and entropy generation simultaneously. The present study combines: (i) 3D Blasius/Sakiadis flow, Casson rheology, Darcy-Forchheimer porous drag, thermal/solutal stratification, and current-aligned/current-reversed MHD forcing within a single formulation; (ii) a signed-Lorentz-force reduced model for $M < 0$ (Eqs. (8)-(9)), with the $M > 0$ case derived from first principles (Eqs. (10)-(14)) and the $M < 0$ case introduced as a postulate, since a literal field reversal does not give the same reduced form; and (iii) an entropy generation analysis (Section 5) quantifying how reversing the current direction affects irreversibility relative to the conventional current-aligned case in both flow configurations. This distinguishes the present contribution from prior MHD Blasius/Sakiadis and Casson-nanofluid studies, which are recovered here as the $M > 0$ special case.

## 2 Mathematical formulation

In this study, the effects of current-aligned ($M > 0$) and current-reversed ($M < 0$) electromagnetic forcing on a 3D Blasius and Sakiadis flow of Casson nanofluid are analyzed, using the signed-Lorentz-force reduced model detailed below (Eqs. (8)-(9)), with the electrical conductivity $\sigma_f > 0$ held fixed in both cases. The general boundary value problem is formulated using four velocity-ratio parameters, $\lambda_1, \lambda_2, \lambda_3, \lambda_4$: $\lambda_1, \lambda_2$ set the wall velocity components ($v_{1_w} = a\lambda_1 x$, $v_{2_w} = a\lambda_2 y$) and $\lambda_3, \lambda_4$ set the free-stream/ambient velocity components ($V_1 = a\lambda_3 x$, $V_2 = a\lambda_4 y$), each normalized by the common stretching rate $a$. Only two special combinations of these four parameters are used in all numerical results reported in this paper: *Blasius flow* (stationary wall, moving ambient fluid), $\lambda_1 = \lambda_2 = 0$, $\lambda_3 = \lambda_4 = 1$; and *Sakiadis flow* (moving wall, quiescent ambient fluid), $\lambda_1 = \lambda_2 = 1$, $\lambda_3 = \lambda_4 = 0$; as shown below, this symmetric choice ($\lambda_1 = \lambda_2$, $\lambda_3 = \lambda_4$, giving $\varphi_1 \equiv \varphi_2$) is required for the self-similarity of the energy and concentration equations (4)-(5). Inertia coefficient of porous medium in $x$ and $y$ directions are taken as $F_1 = \dfrac{c_b}{x\sqrt{K_1}}$ and $F_2 = \dfrac{c_b}{y\sqrt{K_1}}$ respectively; under the similarity transformation ($v_1 = ax\varphi_1'$, $v_2 = ay\varphi_2'$), $F_1(v_1^2 - V_1^2)/(a^2 x)$ and $F_2(v_2^2 - V_2^2)/(a^2 y)$ both reduce to the same dimensionless coefficient $Fr = c_b/\sqrt{K_1}$ (with $c_b$ of dimension length, so that $F_1$ and $F_2$ have dimension $\mathrm{m}^{-1}$) multiplying $(\varphi_1'^2 - \lambda_3^2)$ and $(\varphi_2'^2 - \lambda_4^2)$ respectively in Eqs. (15)-(16), so that a single Forchheimer parameter $Fr$ suffices for both directions. The Casson parameter $\beta$, appearing below through the effective-viscosity factor $(1 + 1/\beta)$, is as defined in the Introduction ($\beta = \mu_B\sqrt{2\pi_c}/\tau_0$); in the limit $\beta \to \infty$ the factor $(1 + 1/\beta) \to 1$ and the classical Newtonian viscous term is recovered. Throughout this paper, "increasing $\beta$" therefore consistently denotes weakening of the non-Newtonian effect, approaching Newtonian behaviour. The system of nanofluid governing equations, along with the boundary restrictions, is formulated following [25, 33, 34, 27, 28]:

$$v_{1x} + v_{2y} + v_{3z} = 0, \tag{1}$$

$$\begin{aligned} v_1 v_{1x} + v_2 v_{1y} + v_3 v_{1z} = {} & \nu_f \left(1 + \frac{1}{\beta}\right) v_{1zz} + V_1 V_{1x} \\ & + V_2 V_{1y} - \frac{\nu_f}{K_1}(v_1 - V_1) - F_1(v_1^2 - V_1^2) - s_M \frac{\sigma_f B_0^2}{\rho_f}(v_1 - V_1), \end{aligned} \tag{2}$$

$$\begin{aligned} v_1 v_{2x} + v_2 v_{2y} + v_3 v_{2z} = {} & \nu_f \left(1 + \frac{1}{\beta}\right) v_{2zz} + V_1 V_{2x} \\ & + V_2 V_{2y} - \frac{\nu_f}{K_1}(v_2 - V_2) - F_2(v_2^2 - V_2^2) - s_M \frac{\sigma_f B_0^2}{\rho_f}(v_2 - V_2), \end{aligned} \tag{3}$$

$$v_1 \alpha_x + v_2 \alpha_y + v_3 \alpha_z = \alpha_f \alpha_{zz} + \kappa \left(B_d \alpha_z C_z + A_d \alpha_z^2\right) + q''' \tag{4}$$

$$v_1 C_x + v_2 C_y + v_3 C_z = B_d C_{zz} + A_d \alpha_{zz} \tag{5}$$

$$\left.\begin{aligned} v_1 = v_{1w}, \quad v_2 = v_{2w}, \quad v_3 = 0, \quad \alpha = \alpha_w, \quad C = C_w \quad at \quad z = 0 \\ v_1 = V_1, \quad v_2 = V_2, \quad \alpha \to \alpha_\infty, \quad C \to C_\infty \quad at \quad z \to \infty \end{aligned}\right\}. \tag{6}$$

Here $\alpha$ denotes the dimensional fluid temperature (equivalently $T$; $T_\infty$ is used in Section 5 as the reference absolute temperature), and $C$ is the nanoparticle volume fraction. The diffusion coefficient in Eq. (4) is the thermal diffusivity $\alpha_f$, $\kappa = (\rho c_p)_s/(\rho c_p)_f$ is the nanoparticle-to-base-fluid heat-capacity ratio, $B_d$ is the Brownian diffusion coefficient, and $A_d = T_d/\alpha_\infty$ is the thermophoretic diffusion parameter, with $T_d$ the thermophoretic diffusion coefficient of the Buongiorno model [15]. In the entropy-generation expression of Section 5, $R$ is the specific gas constant and $D \equiv B_d$ the solutal diffusion coefficient. This mass-diffusion term originates in the entropy-generation theory for ideal-gas species and is adopted here for the nanoparticle suspension, as in the cited stretching-sheet nanofluid studies [25, 33, 34, 27, 28], as a modelling convention. Viscous and Joule heating are omitted from the energy equation (4), as is standard for the low-Eckert-number regime of the cited stretching-sheet models; they are retained in the entropy-generation expression of Section 5, where they act as irreversibility sources, with unit illustrative prefactors that do not represent a specific Eckert number.

The current density $\mathbf{J}$ within the system is governed by:

$$\mathbf{J} = \sigma_f(\mathbf{E} + \mathbf{v} \times \mathbf{B}_0), \tag{7}$$

where $\sigma_f$ denotes the nanofluid's electrical conductivity.

**The signed-Lorentz-force model.** The electromagnetic body force entering the momentum equations (2)-(3) is taken as

$$\mathbf{F}_L = -s_M \sigma_f B_0^2(\mathbf{v} - \mathbf{V}), \qquad s_M = \pm 1, \tag{8}$$

with the corresponding signed magnetic parameter

$$M \equiv s_M \frac{\sigma_f B_0^2}{\rho_f a}, \qquad \sigma_f > 0 \text{ always}, \tag{9}$$

so that $M > 0 \Leftrightarrow s_M = +1$ (current-aligned) and $M < 0 \Leftrightarrow s_M = -1$ (current-reversed); $M_J \equiv |M| = \sigma_f B_0^2/(\rho_f a)$ denotes the corresponding Joule-dissipation magnitude used in Section 5, with $M = s_M M_J$. The $s_M = +1$ case is derived from first principles below and recovers the conventional Lorentz-retarding force; $s_M = -1$ reverses its sign while keeping the relative-velocity structure $(\mathbf{v} - \mathbf{V})$ unchanged, representing an externally driven current opposing the reference direction rather than a literal reversal of the applied electric field (which instead gives $\mathbf{F}_L \propto -(\mathbf{v} + \mathbf{V})$, a qualitatively different, non-vanishing-at-$\mathbf{v} = \mathbf{V}$ force not used here). This signed-forcing configuration – an externally imposed electric field driving a current against or with a fixed magnetic field – is distinct from purely magnetic-field-induced Lorentz braking (the classical Hartmann-flow case with $\mathbf{E} = \mathbf{0}$, which only ever retards the flow).

**Derivation of the $s_M = +1$ case.** Under the standard low-magnetic-Reynolds-number (quasi-static) approximation used throughout the boundary-layer MHD literature [25, 33, 34, 27, 28], the induced magnetic field is negligible and the applied field is normal to the sheet, $\mathbf{B}_0 = B_0\hat{\mathbf{e}}_z$, uniform (the applied magnetic flux density $B_0$ is unrelated to the stratification coefficient $B$ of Section 1). Within the boundary layer $\mathbf{v} = (v_1, v_2, 0)$ satisfies $\mathbf{v}\cdot\mathbf{B}_0 = 0$. Taking the electric field in the frame co-moving with the reference velocity $\mathbf{V} = (V_1, V_2, 0)$,

$$\mathbf{E} = -\mathbf{V}\times\mathbf{B}_0, \tag{10}$$

which is precisely the condition under which the induced current vanishes as $\mathbf{v}\to\mathbf{V}$, in particular as $z\to\infty$ where boundary conditions (6) require this. Substituting into Ohm's law (7),

$$\mathbf{J} = \sigma_f\big[(\mathbf{v}-\mathbf{V})\times\mathbf{B}_0\big], \tag{11}$$

so that the Lorentz force per unit volume is

$$\mathbf{F}_L = \mathbf{J}\times\mathbf{B}_0 = \sigma_f\big[(\mathbf{v}-\mathbf{V})\times\mathbf{B}_0\big]\times\mathbf{B}_0. \tag{12}$$

Using $(\mathbf{A}\times\mathbf{B}_0)\times\mathbf{B}_0 = \mathbf{B}_0(\mathbf{A}\cdot\mathbf{B}_0) - \mathbf{A}\,|\mathbf{B}_0|^2$ and $(\mathbf{v}-\mathbf{V})\cdot\mathbf{B}_0 = 0$, Eq. (12) reduces to

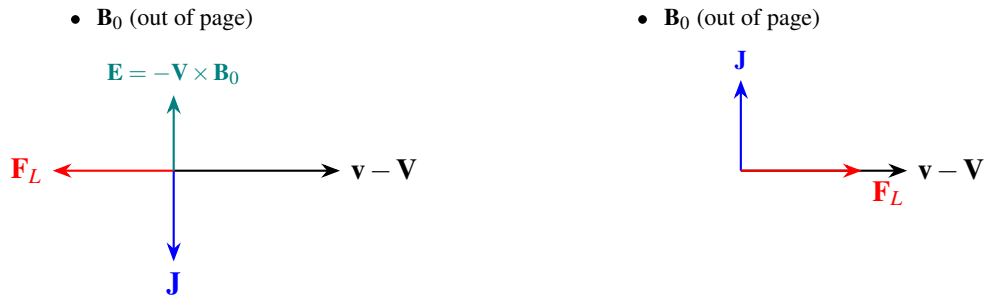
$$\mathbf{F}_L = -\sigma_f B_0^2(\mathbf{v}-\mathbf{V}), \tag{13}$$

i.e. Eq. (8) with $s_M = +1$: component-wise, $F_{L,x} = -\sigma_f B_0^2(v_1 - V_1)$, $F_{L,y} = -\sigma_f B_0^2(v_2 - V_2)$, with no cross-coupling between directions, matching Eqs. (2)-(3). Introducing the similarity variables $v_1 = ax\varphi_1'$, $V_1 = a\lambda_3 x$ and dividing by $ax$ gives

$$\frac{F_{L,x}}{\rho_f a x} = -\frac{\sigma_f B_0^2}{\rho_f a}(\varphi_1' - \lambda_3) = -M(\varphi_1' - \lambda_3), \qquad M = \frac{\sigma_f B_0^2}{\rho_f a} > 0, \tag{14}$$

the electromagnetic term in Eq. (15) (and analogously Eq. (16)); for $M < 0$, the sign of this coefficient is flipped while $(\varphi_1' - \lambda_3)$ and $\sigma_f > 0$ are unchanged, following the quasi-1D, decoupled-direction reduction used in the cited works [25, 33, 34, 27, 28].

**Physical mechanism and realizability of the accelerating ($M < 0$) regime.** For $M < 0$ ($s_M = -1$), the electromagnetic term $-M(\varphi_1' - \lambda_3)$ in Eq. (15) changes sign relative to the $M > 0$ case: where the current-aligned configuration retards the flow towards the reference velocity, the current-reversed configuration accelerates it away from that reference. Three energy channels are involved: (i) the electromagnetic work rate relative to the reference flow, $\mathbf{F}_L\cdot(\mathbf{v}-\mathbf{V}) = -s_M\sigma_f B_0^2|\mathbf{v}-\mathbf{V}|^2$, is *reversible* and signed – negative (braking) for $s_M = +1$, positive (driving) for $s_M = -1$ – and is the channel through which kinetic energy of the relative flow is added or removed by the external field (the work $\mathbf{F}_L\cdot\mathbf{v}$ on the absolute kinetic energy also depends on $\mathbf{V}$ and is not signed by $s_M$ alone); (ii) Ohmic dissipation $\mathbf{J}\cdot\mathbf{E}' = |\mathbf{J}|^2/\sigma_f$ (Eq. (25)) is *irreversible* and strictly non-negative regardless of $s_M$, since it depends only on $|\mathbf{J}|^2$; (iii) viscous dissipation $\Phi_{visc} = \mu_f(1+1/\beta)[(v_{1z})^2 + (v_{2z})^2]$ is likewise irreversible and sign-independent. For $M < 0$, the kinetic energy added to the flow via




**(a)** $M > 0$ **(current-aligned)**

$\mathbf{F}_L = -\sigma_f B_0^2(\mathbf{v} - \mathbf{V})$

retards flow

**(b)** $M < 0$ **(current-reversed)**

$\mathbf{F}_L = +\sigma_f B_0^2(\mathbf{v} - \mathbf{V})$

accelerates flow

Fig. 1 – Schematic of the signed-Lorentz-force model (Eq. (8)) for a fixed relative velocity $\mathbf{v} - \mathbf{V}$ and applied field $\mathbf{B}_0$ out of the page. (a) $M > 0$: $\mathbf{F}_L$ opposes $\mathbf{v} - \mathbf{V}$, retarding the flow. (b) $M < 0$: $\mathbf{J}$ and $\mathbf{F}_L$ are reversed, so $\mathbf{F}_L$ reinforces $\mathbf{v} - \mathbf{V}$, accelerating the flow.

(i) is supplied externally by the source maintaining the imposed field configuration, analogous in spirit to an MHD accelerator/pump operating in driving rather than braking mode; the corresponding source-power term is not modelled here, and Section 5 quantifies the associated irreversibility. Such configurations are conceptually related to MHD pumping and electromagnetic flow-control devices; the present study is a numerical investigation of the reduced model of Eq. (8).

The heat generation/absorption term $q'''$ in Eq. (4), following prior related literature [25, 33, 34, 27, 28], is given by

$$q''' = \frac{Q}{\rho c_p}(\alpha - \alpha_\infty),$$

where $Q$ is the dimensional volumetric heat-generation/absorption coefficient, with corresponding dimensionless parameter $Q^* = Q/(a\rho c_p)$ (Table 2). The boundary conditions for temperature and concentration are specified as:

$$\begin{aligned} \alpha_w &= T_0 + A(x+y), \\ \alpha_\infty &= T_0 + B(x+y), \\ C_w &= C_0 + E(x+y), \\ C_\infty &= C_0 + F(x+y), \end{aligned}$$

representing wall temperature, ambient temperature, wall concentration, and ambient concentration respectively, with $A, B, E, F > 0$ throughout this paper (both wall and ambient temperature/concentration increase linearly with $x+y$, as is standard for the stratified-flow literature [25, 33, 34, 27, 28]); the statements in Section 4 regarding the direction in which $St = B/A$ and $Ss = F/E$ shift the wall-to-ambient difference assume this sign convention and would need re-examination if $A, B, E, F$ were allowed to take other signs. The governing partial differential equations

are reduced to ordinary differential equations through the following similarity transformations:

$$v_1 = ax\varphi_1', \quad v_2 = ay\varphi_2', \quad v_3 = -\sqrt{a\nu}(\varphi_1+\varphi_2),$$
$$\varphi_3 = \frac{\alpha-\alpha_\infty}{\alpha_w-T_0}, \quad \varphi_4 = \frac{C-C_\infty}{C_w-C_0}, \quad \eta = \sqrt{\frac{a}{\nu}}z$$

Here $C$ denotes the dimensional nanoparticle volume fraction field (as defined above), kept notationally distinct from the Casson (non-Newtonian) parameter $\beta$ appearing in Eqs. (2)-(3) and (15)-(16). This normalization (by $\alpha_w - T_0 = A(x+y)$ and $C_w - C_0 = E(x+y)$, rather than by $\alpha_w - \alpha_\infty$ and $C_w - C_\infty$) is the one consistent with the wall boundary conditions used throughout this paper: at $\eta = 0$, $\alpha = \alpha_w$ and $C = C_w$, so $\varphi_3(0) = (\alpha_w - \alpha_\infty)/(\alpha_w - T_0) = (A-B)/A = 1 - St$ and $\varphi_4(0) = (C_w - C_\infty)/(C_w - C_0) = (E-F)/E = 1 - Ss$, as imposed in Eq. (19).

**Similarity reduction.** Introducing the similarity variables stated above, together with the symmetric restriction $\varphi_1 \equiv \varphi_2 \equiv \varphi$ required by the Blasius/Sakiadis configurations of this paper ($\lambda_1 = \lambda_2$, $\lambda_3 = \lambda_4$) and the rescaling $B_d = B_{d0}/(x+y)$, $A_d = A_{d0}/(x+y)$ needed for the diffusion coefficients to remain $(x,y)$-independent, transforms Eqs. (1)-(6) into the dimensionless system below, following the same reduction procedure used throughout the stratified-stretching-sheet literature [25, 33, 34, 27, 28]. The resulting coupled ordinary differential equations are

$$\left(1+\frac{1}{\beta}\right)\varphi_{1\eta\eta\eta} + (\varphi_1+\varphi_2)\varphi_{1\eta\eta} - \left(\frac{1}{Da}+M\right)(\varphi_{1\eta}-\lambda_3) - Fr(\varphi_{1\eta}^2 - \lambda_3^2) + \lambda_3^2 - \varphi_{1\eta}^2 = 0 \quad (15)$$

$$\left(1+\frac{1}{\beta}\right)\varphi_{2\eta\eta\eta} + (\varphi_1+\varphi_2)\varphi_{2\eta\eta} - \left(\frac{1}{Da}+M\right)(\varphi_{2\eta}-\lambda_4) - Fr(\varphi_{2\eta}^2 - \lambda_4^2) + \lambda_4^2 - \varphi_{2\eta}^2 = 0 \quad (16)$$

$$\varphi_3'' + Pr[Nb\varphi_4' + Nt\varphi_3']\varphi_3' + Pr(\varphi_1+\varphi_2)\varphi_3' + Q^*\varphi_3 = Pr(\varphi_3+St)(\varphi_1'+\varphi_2') \quad (17)$$

$$\varphi_4'' + Sc(\varphi_1+\varphi_2)\varphi_4' + Nr\varphi_3'' = Sc(\varphi_1'+\varphi_2')(\varphi_4+Ss) \quad (18)$$

The deduced restrictions are

$$\left.\begin{array}{r}(\varphi_1+\varphi_2)(\eta)=0,\ \ \varphi_1'(\eta)=\lambda_1,\ \ \varphi_2'(\eta)=\lambda_2,\ \ \varphi_3(\eta)=1-St,\ \ \varphi_4(\eta)=1-Ss,\ \text{ as }\ \eta\to 0\\ \varphi_1'(\eta)=\lambda_3,\ \ \varphi_2'(\eta)=\lambda_4,\ \ \varphi_3(\eta)=0,\ \ \varphi_4(\eta)=0,\ \text{ as }\ \eta\to\infty\end{array}\right\}. \quad (19)$$

Throughout the Results (Section 4) and in Table 4, the two flow configurations correspond to the following standard choice of the wall/free-stream velocity-ratio parameters $\lambda_1, \lambda_2, \lambda_3, \lambda_4$: for *Blasius flow* (stationary sheet, moving ambient fluid), $\lambda_1 = \lambda_2 = 0$ and $\lambda_3 = \lambda_4 = 1$; for *Sakiadis flow* (moving sheet, quiescent ambient fluid), $\lambda_1 = \lambda_2 = 1$ and $\lambda_3 = \lambda_4 = 0$. Unless otherwise stated, results are

reported for $|M| = 3$ (i.e. $M = 3$ for the current-aligned case and $M = -3$ for the current-reversed case), with the sign of $M$ stated in each figure and table. Notations and dimensionless parameters

$$\kappa = \frac{(\rho c_p)_s}{(\rho c_p)_f}, \qquad A_d = \frac{T_d}{\alpha_\infty}, \qquad Da = \frac{aK_1}{\nu_f}, \qquad Q^* = \frac{Q}{a\rho c_p},$$
$$Nt = \frac{\kappa A_d(\alpha_w - T_0)}{\nu_f}, \qquad Nb = \frac{\kappa B_d(C_w - C_0)}{\nu_f}, \qquad Nr = \frac{Nt}{Nb}, \qquad M = s_M \frac{\sigma_f B_0^2}{\rho_f a},$$
$$Sc = \frac{\nu_f}{B_d}, \qquad Fr = \frac{c_b}{\sqrt{K_1}}, \qquad Pr = \frac{\nu_f}{\alpha_f}, \qquad St = \frac{B}{A}, \quad Ss = \frac{F}{E}. \tag{20}$$

In the Buongiorno model [15], $Nb$ and $Nt$ arise from the Brownian- and thermophoretic-diffusion

Table 1 – Nomenclature: dimensional quantities, SI units, and physical interpretation.

| Symbol | SI units | Physical interpretation |
|---|---|---|
| $x, y, z$ | m | Cartesian coordinates (streamwise, spanwise, wall-normal) |
| $v_1, v_2, v_3$ | $\mathrm{m\,s^{-1}}$ | velocity components in $x, y, z$ |
| $a$ | $\mathrm{s^{-1}}$ | common stretching/shrinking rate of the wall/free-stream |
| $\alpha$ (or $T$) | K | dimensional fluid temperature |
| $C$ | – (dimensionless) | nanoparticle volume fraction |
| $\rho_f$ | $\mathrm{kg\,m^{-3}}$ | base-fluid density |
| $\mu_f$, $\mu_B$ | Pa s | dynamic viscosity; Casson plastic dynamic viscosity |
| $\nu_f = \mu_f/\rho_f$ | $\mathrm{m^2\,s^{-1}}$ | kinematic viscosity |
| $\tau_0$ | Pa | Casson yield stress |
| $k_f$ | $\mathrm{W\,m^{-1}\,K^{-1}}$ | thermal conductivity of the base fluid |
| $c_p$ | $\mathrm{J\,kg^{-1}\,K^{-1}}$ | specific heat capacity |
| $\alpha_f = k_f/(\rho c_p)_f$ | $\mathrm{m^2\,s^{-1}}$ | thermal diffusivity |
| $\sigma_f$ | $\mathrm{S\,m^{-1}}$ | electrical conductivity (positive throughout) |
| $B_0$ | T | applied magnetic flux density |
| $K_1$ | $\mathrm{m^2}$ | porous-medium permeability |
| $c_b$ | m | Forchheimer (inertial drag) coefficient |
| $B_d$ | $\mathrm{m^2\,s^{-1}}$ | Brownian diffusion coefficient |
| $T_d$ | $\mathrm{m^2\,s^{-1}}$ | thermophoretic diffusion coefficient |
| $Q$ | $\mathrm{W\,m^{-3}\,K^{-1}}$ | volumetric heat-generation/absorption coefficient |
| $R$ | $\mathrm{J\,kg^{-1}\,K^{-1}}$ | specific gas constant (entropy-generation model, Section 5) |
| $D \equiv B_d$ | $\mathrm{m^2\,s^{-1}}$ | solutal (Brownian) diffusion coefficient (entropy-generation model) |
| $T_\infty$ | K | reference (ambient) absolute temperature (entropy-generation model) |
| $A, B$ | $\mathrm{K\,m^{-1}}$ | wall/ambient temperature stratification coefficients ($A, B > 0$) |
| $E, F$ | $\mathrm{m^{-1}}$ | wall/ambient concentration stratification coefficients ($E, F > 0$) |
| $\eta$ | – (dimensionless) | similarity coordinate, $\eta = z\sqrt{a/\nu_f}$ |

flux terms in the nanoparticle conservation equation (Eq. (5)) and are typically small ($O(10^{-2})$–$O(1)$) for dilute suspensions. The value $Nt = 0.02$ lies well within this range, whereas $Nb = 0.5$ is at its upper end and is chosen to make the Brownian-diffusion sensitivity visible in Table 4;

Table 2 – Dimensionless parameters: definitions, default value, investigated range, and physical/literature justification.

| Symbol | Definition | Default | Range tested | Justification |
|---|---|---|---|---|
| $M$ | $s_M\sigma_f B_0^2/(\rho_f a)$ | $\pm 3$ | $-5$ to 5 | Typical Hartmann-type range for stretching-sheet MHD nanofluid studies [25, 33, 34, 27, 28]; sign fixed by $s_M$ (Eq. (9)) |
| $Da$ | $aK_1/\nu_f$ | 0.63 | 0.53–0.73 | $O(1)$ Darcy number typical of moderately permeable porous media in this literature [25, 27] |
| $Fr$ | $c_b/\sqrt{K_1}$ | 0.2 | 0.1–0.3 | Small-to-moderate inertial correction, consistent with Forchheimer-extended Darcy studies [27] |
| $\beta$ | – | 2 | $1,2,3,5$ | Moderate non-Newtonian (Casson) effect, within the range used for blood/polymer-type fluids [21] |
| $Pr$ | $\nu_f/\alpha_f$ | 6.07 | fixed | Representative of a water-based base fluid at room temperature |
| $Sc$ | $\nu_f/B_d$ | 2 | 1–3 | Typical range for nanoparticle Brownian diffusion in a liquid base fluid [15] |
| $Nb$ | $\kappa B_d(C_w - C_0)/\nu_f$ | 0.5 | 0.4–0.6 | Upper end of the dilute-suspension range; chosen for sensitivity, see discussion below |
| $Nt$ | $\kappa A_d(\alpha_w - T_0)/\nu_f$ | 0.02 | 0.01–0.03 | Small, consistent with weak thermophoretic diffusion relative to Brownian diffusion [15] |
| $Nr$ | $Nt/Nb$ | 0.04 | – | Follows from $Nb, Nt$ above; $Nr \ll 1$ as expected |
| $Q^*$ | $Q/(a\rho c_p)$ | 5 | fixed | Chosen to be strongly heat-generating specifically to stress-test domain independence (Section 4.1); not intended as representative of a specific physical heat source |
| $St$ | $B/A$ | 3 | fixed | Illustrative moderate-to-strong stratification, as commonly used in this literature [25, 33, 34, 27, 28] |
| $Ss$ | $F/E$ | 3 | fixed | As for $St$ above |
| $\kappa$ | $(\rho c_p)_s/(\rho c_p)_f$ | – | – | Material property ratio; not independently varied |
| $A_d$ | $T_d/\alpha_\infty$ | – | – | Enters only through $Nt$ above |
| $\lambda_1, \lambda_2$ | – | 0 or 1 | B/S | Flow-configuration convention (Section 2) |
| $\lambda_3, \lambda_4$ | – | 1 or 0 | B/S | Flow-configuration convention (Section 2) |

$Nr = Nt/Nb \ll 1$ reflects weak thermophoretic relative to Brownian diffusion. The value $Q^* = 5$ is deliberately large, to test the domain-independence behaviour of Section 4.1. The remaining parameters $(Da, Fr, M, Sc, \beta, St, Ss)$ lie within ranges commonly used in the cited literature [25, 33, 34, 27, 28]. The study is a dimensionless parametric investigation and does not refer to a specific nanofluid. In a real nanofluid, the electrical conductivity $\sigma_f$ is a positive material property; a negative value has no conventional physical meaning for a passive conducting medium, and the reduced model of Eq. (8)-(9) does not require it: $\sigma_f > 0$ is retained throughout, and the sign of $M$ enters only through $s_M$. Under the current-reversed ($M < 0$, $s_M = -1$) configuration, $\mathbf{J} \to -\mathbf{J}$ relative to the $M > 0$ reference direction, so "current-reversed" here denotes current flowing opposite to that reference, not a spon-

taneously active or non-equilibrium medium; the associated Ohmic dissipation $\mathbf{J}\cdot\mathbf{E}' = |\mathbf{J}|^2/\sigma_f \geq 0$ (with $\mathbf{E}' = \mathbf{J}/\sigma_f$ the field in the fluid's frame, Section 5) is unaffected by this sign reversal, since it depends only on $|\mathbf{J}|^2$, not on $s_M$.

# 3 Numerical Methodology

## Problem Transformation

The governing boundary value problem (BVP), consisting of Equations (15)-(18) with boundary conditions (19), requires special numerical treatment due to its coupled nonlinear nature. We employ a dual transformation strategy. Throughout this paper, the subscript-$\eta$ notation ($\varphi_{1\eta}$, $\varphi_{1\eta\eta}$, etc.) and the prime notation ($\varphi_1'$, $\varphi_1''$, etc.) both denote ordinary differentiation with respect to the similarity variable $\eta$ and are used interchangeably ($\varphi_{1\eta} \equiv \varphi_1'$, $\varphi_{1\eta\eta} \equiv \varphi_1''$); the subscript form is used here for the order-reduction bookkeeping, and the prime form is used elsewhere for compactness.

1. **Order Reduction:** Convert all third-order ODEs to first-order systems through the substitutions:

$$\begin{aligned} &\varphi_1 = X_1, \quad \varphi_{1\eta} = X_2, \quad \varphi_{1\eta\eta} = X_3 \\ &\varphi_2 = X_4, \quad \varphi_{2\eta} = X_5, \quad \varphi_{2\eta\eta} = X_6 \\ &\varphi_3 = X_7, \quad \varphi_{3\eta} = X_8 \\ &\varphi_4 = X_9, \quad \varphi_{4\eta} = X_{10} \end{aligned}$$

2. **BVP to IVP Conversion:** Implement shooting method by guessing initial conditions for missing boundary values:

$$X_3(0) = \alpha_1, \quad X_6(0) = \alpha_2, \quad X_8(0) = \alpha_3, \quad X_{10}(0) = \alpha_4$$

## Adaptive Runge-Kutta-Newton Framework

The solution process combines two powerful numerical techniques:

- **RK45 Integration:** Solve the transformed initial value problem (IVP) using adaptive 4th/5th order Runge-Kutta method with:
  - Absolute tolerance: $10^{-6}$
  - Relative tolerance: $10^{-4}$
  - Automatic step-size adjustment
- **Newton-Raphson Correction:** Iteratively refine initial guesses through:

$$\alpha^{(k+1)} = \alpha^{(k)} - \mathbf{J}^{-1}\mathbf{F}(\alpha^{(k)})$$

where $\mathbf{J}$ is the Jacobian matrix of boundary residuals and $\mathbf{F}$ contains the mismatch at $\eta_\infty$. The Jacobian is evaluated by forward finite differences (perturbing each component of $\alpha$ by $10^{-6}$ relative to its magnitude and re-integrating the IVP), not analytically. A maximum of 50 Newton iterations is allowed per parameter step; if the residual has not met the tolerance of Eq. (21) within this limit, the step is treated as a failed iteration: the parameter increment is halved and the correction is retried from the last converged solution (standard damped/backtracking continuation), up to 5 halvings, after which the parameter point is reported as non-convergent rather than iterated further.

## Convergence Protocol

The algorithm proceeds as follows:

1. Initialize with $\eta_\infty = 10$ (sufficient for asymptotic convergence)
2. Compute solutions for progressively larger $\eta_\infty$ until relative changes in:

$$\max(|\varphi_1'(\eta_\infty) - \lambda_3|, |\varphi_2'(\eta_\infty) - \lambda_4|) < 10^{-5}$$

3. Finalize when all boundary residuals satisfy:

$$\|\mathbf{F}(\alpha)\|_2 < 10^{-6} \tag{21}$$

Following this protocol, $\eta_\infty = 10$ was found sufficient for the momentum field in the representative cases tested (see the domain-independence refinement in Section 4.1 regarding thermal/concentration gradients under strong heat generation); the Newton-Raphson correction typically converges within 4–6 iterations from the initial guess. In practice, the achieved residual is typically one to five orders of magnitude tighter than this $10^{-6}$ target: the domain-independence checks of Section 4.1 (Table 6) were run at solver tolerance $10^{-10}$ with reported maximum residuals of order $10^{-9}$–$10^{-11}$; the coupled thermal/concentration checks of Table 8 were run at tolerance $10^{-8}$ with maximum residuals of order $10^{-8}$–$10^{-9}$ (tabulated there); and the manufactured-solution and MHD-Darcy exact-solution benchmarks of Section 4.2 achieved errors of $10^{-7}$ and $10^{-13}$ respectively against their known reference solutions.

## Branch Selection

Since the underlying boundary value problem may admit multiple solution branches in parts of parameter space [27], the physically relevant branch is selected by continuation: starting from a converged solution at a nearby parameter value (or from the limiting-case profile of Section 4.1 where available), each parameter is stepped in small increments (typically $\Delta M = 0.5$ for the $M$-sweeps of Sections 4.1 and 5, $\Delta Sc = 0.1$ for the Schmidt-number continuation of Section 5; other parameters are stepped as shown in Table 4) using the previous solution as the initial guess. A candidate solution is accepted only if it is bounded on $[0, \eta_\infty]$, satisfies the residual tolerance of Eq. (21), and approaches

the prescribed far-field values. Overshoots and sign changes of $\varphi_3$ and $\varphi_4$ (as for $M < 0$, or from heat generation) are admissible when the ODEs and boundary conditions are satisfied. Monotonic decay is used only as a heuristic to discriminate between competing branches, not as a physical requirement on the stratified variables. The selection does not establish stability or uniqueness of the chosen branch, nor that competing branches are unstable. Branches failing these checks are reported as non-convergent within the present scheme rather than as proven spurious. A full linear-stability, bifurcation, or systematic branch-tracking analysis of possible multiple-solution behavior has not been performed and is beyond the present scope.

### Computational Advantages

This hybrid approach offers three key benefits:

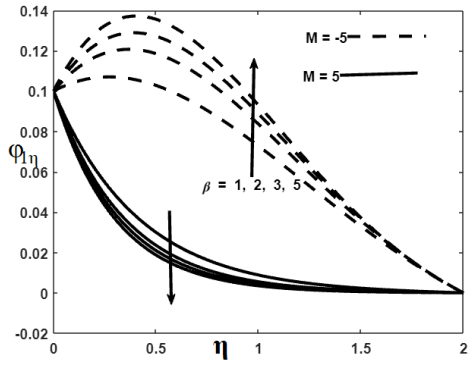
- **Precision:** the embedded 4th/5th-order Runge-Kutta pair (RK45) advances the solution using the 5th-order estimate; for a $p$-th order method, the per-step (local) truncation error is $O(h^{p+1})$ and the accumulated (global) error is $O(h^p)$, so the 5th-order estimate used here has local error $O(h^6)$ and global error $O(h^5)$. The 4th-order estimate is used only, via the difference between the two estimates, for adaptive step-size control. This ensures accurate gradient calculations for Newton iterations
- **Efficiency:** Adaptive stepping minimizes function evaluations in regions of low nonlinearity
- **Robustness:** Newton corrections prevent solution divergence common in pure shooting methods

### Entropy Generation Computation

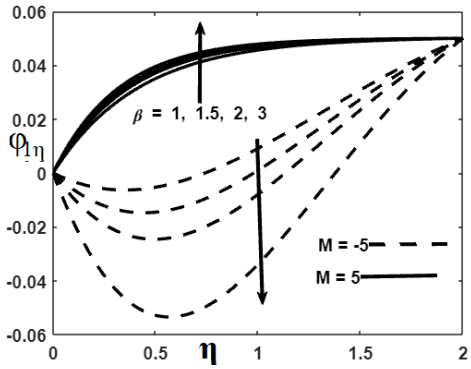
Once the boundary value problem (15)-(19) is solved and the converged profiles $\varphi_1, \varphi_2, \varphi_3, \varphi_4$ and their derivatives are obtained, the entropy generation number $Ns$ and Bejan number $Be$ are evaluated as a direct post-processing step from the same solution, without any additional shooting or re-solving. The full formulation of $Ns$ and $Be$, together with the physical justification for using $|M|$ in the Joule-heating term, is given in Section 5.

## 4 Results and Discussion

Unless a parameter is the one being varied in a given figure, the following default values are held fixed throughout this section: $Da = 0.63$, $Fr = 0.2$, $|M| = 3$, $Pr = 6.07$, $Nb = 0.5$, $Nt = 0.02$, $Q^* = 5$, $Sc = 2$, $St = Ss = 3$, with the $\lambda_i$ convention of Section 2 ($\lambda_1 = \lambda_2 = 0, \lambda_3 = \lambda_4 = 1$ for Blasius; $\lambda_1 = \lambda_2 = 1, \lambda_3 = \lambda_4 = 0$ for Sakiadis). In every figure showing both signs of $M$, the solid line corresponds to $M > 0$ (current-aligned) and the dashed line to $M < 0$ (current-reversed); $|M| = 5$ in Figs. 2a–4b and $|M| = 3$ in the tables and entropy figures. Figs. 2a-4b are computed for $M = \pm 5$ with $\lambda_3 = 0.05$ (Blasius) and $\lambda_1 = 0.1$ (Sakiadis), the remaining parameters being held at the defaults




(a) Effect of $\varphi_1'$ and $\varphi_2'$ with $\beta$ in Sakiadis flow.




(b) Effect of $\varphi_1'$ and $\varphi_2'$ with $\beta$ in Blasius flow.

Fig. 2 – Effect of $\varphi_1'$ and $\varphi_2'$ with $\beta$ in Blasius and Sakiadis flow when $M > 0$ and $M < 0$.

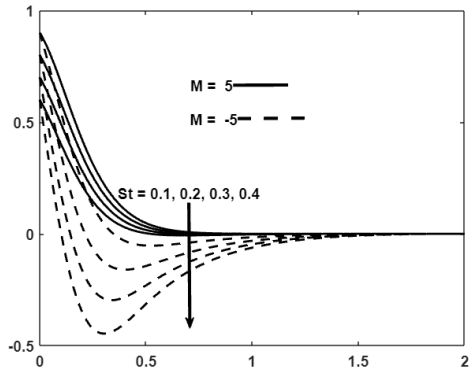
above except where varied: $\beta$ in Figs. 2a–2b, and $St$ and $Ss$ over 0.1–0.4 in Figs. 3a–3b and 4a–4b respectively. The profiles are plotted over $0 \leq \eta \leq 2$, beyond which they are indistinguishable from their far-field values. These figures show the effects of the relevant dimensionless parameters on velocity, temperature, and concentration for $M > 0$ and $M < 0$ in Blasius and Sakiadis nanofluid flows. Figs. 2a and 2b show the effect of $\beta$ on velocity for $M > 0$ and $M < 0$ in Sakiadis and Blasius flow. In Sakiadis flow, increasing $\beta$ decreases velocity for $M > 0$ but increases it for $M < 0$; in Blasius flow, the trend is reversed (enhanced for $M > 0$, decreased for $M < 0$). For $M < 0$ in Blasius flow, $\varphi_1'$ becomes negative near the wall (reverse flow) before recovering to the free-stream value, and in Sakiadis flow it exceeds the wall value, i.e. the fluid is accelerated. These opposite responses follow from the sign of $M$ (current flowing opposite to the $M > 0$ reference for $M < 0$).

Table 3 reports the momentum displacement thickness $\delta^* = \int_0^{\eta_\infty} \left(1 - \varphi_1'/\lambda_3\right) d\eta$ (Blasius) or $\int_0^{\eta_\infty} (\varphi_1'/\lambda_1)\, d\eta$ (Sakiadis) at $\beta = 1, 2, 3, 5$ ($Da = 0.63$, $Fr = 0.2$, $|M| = 3$). For Blasius flow (both signs of $M$) and Sakiadis flow with $M > 0$, $\delta^*$ decreases monotonically with $\beta$, quantitatively confirming the thinning trend. Note that the two definitions of $\delta^*$ use different reference states (the free-stream velocity $\lambda_3$ for Blasius, the wall velocity $\lambda_1$ for Sakiadis, since the other is zero in each case); the values are therefore meaningful indicators of thinning *within* each configuration as $\beta$ varies, but are not directly comparable in magnitude *between* Blasius and Sakiadis.

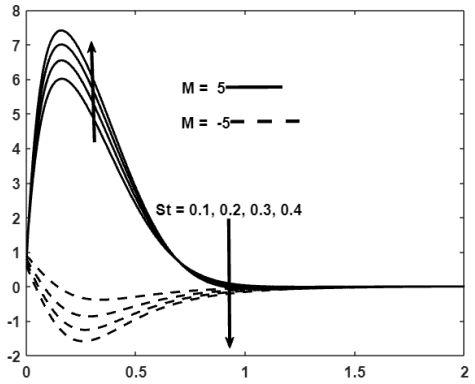
Table 3 – Displacement thickness $\delta^*$ versus $\beta$ (single-direction reduction, $\varphi_2 \equiv 0$; see Section 4.1)

| Case | $\beta = 1$ | $\beta = 2$ | $\beta = 3$ | $\beta = 5$ |
|---|---|---|---|---|
| Blasius, $M = 3$ | 0.521 | 0.451 | 0.425 | 0.403 |
| Blasius, $M = -3$ | 1.311 | 1.135 | 1.070 | 1.016 |
| Sakiadis, $M = 3$ | 0.595 | 0.515 | 0.486 | 0.461 |

Figs. 3a and 3b show the effect of the thermal stratification parameter $St$ on temperature. Increasing

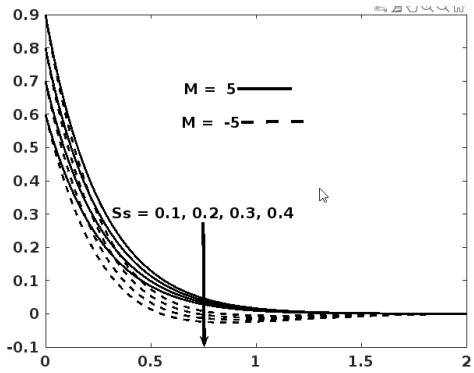



(a) Effect of $\varphi_3$ with $St$ in Sakiadis flow.

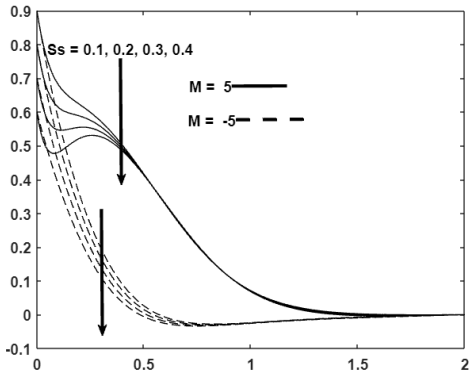



(b) Effect of $\varphi_3$ with $St$ in Blasius flow.

Fig. 3 – Effect of $\varphi_3$ with $St$ in Blasius flow and Sakiadis flow when $M > 0$ and when $M < 0$.




(a) Effect of $\varphi_4$ with $Ss$ in Sakiadis flow.




(b) Effect of $\varphi_4$ with $Ss$ in Blasius flow.

Fig. 4 – Effect of $\varphi_4$ with $Ss$ in Blasius flow and Sakiadis flow when $M > 0$ and when $M < 0$.

$St$ lowers the wall value, $\varphi_3(0) = 1 - St$ (Eq. (19)), in all cases, because $St = B/A$ raises the ambient temperature relative to the wall temperature. In Sakiadis flow with $M > 0$, $\varphi_3$ decreases monotonically with $St$ throughout the layer. In Blasius flow with $M > 0$, $\varphi_3$ rises from the wall to a pronounced maximum near $\eta \approx 0.15$, which grows with $St$, and then decays; beyond $\eta \approx 0.9$ the curves again decrease with $St$. For $M < 0$ the temperature in both flows falls below the ambient value ($\varphi_3 < 0$) over part of the layer, and the undershoot deepens with $St$. The maximum in the Blasius profile (an inflection in the temperature distribution) is consistent with the stationary sheet being crossed by stratified fluid. Magnitude of the $\varphi_{3\eta}$ is higher in Blasius case when $M > 0$.

Figs. 4a and 4b show the effect of concentration with $Ss$ in two cases $M > 0$ and $M < 0$. These variations are checked in both Blasius/Sakiadis flows. $\varphi_{4\eta}$ decreases with $Ss$ (solutal stratification) in both cases, i.e., $M > 0$ and $M < 0$, for Sakiadis and Blasius flows. As with $St$, the wall value is fixed by the formulation: the solutal stratification parameter $Ss = F/E$ enters through $\varphi_4(0) = 1 - Ss$

(Eq. (19)), so that increasing $Ss$ lowers the concentration at the wall and, correspondingly, the profile as a whole. For $M < 0$ the concentration undershoots zero slightly near $\eta \approx 0.8$–1 before approaching the ambient value.

For Table 4, each parameter ($Fr$, $Da$, $Sc$, $Nb$, $Nt$) is varied one at a time over the three listed values while all other parameters are held at the default values stated at the start of this section (Section 4); solutions are obtained by continuation from the nearest previously converged case in the sweep (e.g., $Fr = 0.2 \to 0.1 \to 0.3$), following the Branch Selection procedure of Section 3, rather than independently from a cold-start guess at every value. Table 4 shows that the magnitude of $\varphi_{1\eta\eta}(0)/\varphi_{2\eta\eta}(0)$, $-\varphi_{3\eta}(0)$ and $-\varphi_{4\eta}(0)$ increases with $Fr$ and decreases with $Da$ in Blasius flow. In Sakiadis flow, the trend is similar for $\varphi_{1\eta\eta}(0)/\varphi_{2\eta\eta}(0)$, but $-\varphi_{3\eta}(0)$ and $-\varphi_{4\eta}(0)$ show the opposite trend, decreasing with $Fr$ and increasing with $Da$. $-\varphi_{3\eta}(0)$ and $-\varphi_{4\eta}(0)$ show similar variations with $Sc$ and $Nb$: $-\varphi_{3\eta}(0)$ is reduced while $-\varphi_{4\eta}(0)$ is enhanced with $Sc$ and $Nb$ in both Blasius and Sakiadis flow. With $Nt$, both $-\varphi_{3\eta}(0)$ and $-\varphi_{4\eta}(0)$ are reduced in both Blasius and Sakiadis flows. In terms of magnitude, the effect of $Fr$ on $\varphi_{1\eta\eta}(0)$ is negligible: the relative change is $|\varphi_{1\eta\eta}(0)|_{Fr=0.3} - |\varphi_{1\eta\eta}(0)|_{Fr=0.1}|/|\varphi_{1\eta\eta}(0)|_{Fr=0.1} \approx 1.6 \times 10^{-4}$ (well below 0.1%) across the range tested, and should not be interpreted as a physically significant trend. This is expected directly from Eq. (15): $Fr$ multiplies the quadratic term $(\varphi_1'^2 - \lambda_3^2)$, whereas the linear Darcy/Lorentz coefficient $(1/Da + M) \approx 1/0.63 + 3 \approx 4.6$ is more than an order of magnitude larger than $Fr \in [0.1, 0.3]$ at the default parameters, and $(\varphi_1'^2 - \lambda_3^2)$ itself is small near the wall (where $\varphi_1'(0) = \lambda_1$ is often close to $\lambda_3$) and vanishes in the far field; the $Fr$ term therefore contributes only a small correction to $\varphi_1''(0)$ relative to the dominant linear terms. The effect of $Da$ on $\varphi_{1\eta\eta}(0)$ is small ($\sim$ 2–3%); whereas $Sc$ and $Nb$ produce strong changes in $-\varphi_{3\eta}(0)$ and $-\varphi_{4\eta}(0)$ (up to a factor of $\sim 3$ over the range considered), and $Nt$ produces a moderate change ($\sim$ 10–15%). **Domain convergence:** Table 4 is computed at $\eta_\infty = 10$. As shown in Section 4.1 (Table 9), $\varphi_{1\eta\eta}(0)$ is fully domain-independent at this truncation for every row, but $-\varphi_{3\eta}(0)$ and $-\varphi_{4\eta}(0)$ are not, shifting by $-4$ to $-10\%$ and $+15$ to $+41\%$ respectively at $\eta_\infty = 30$. The qualitative trends (direction of increase/decrease) are unaffected, but the specific values in this table should be read as $\eta_\infty = 10$ values; the domain-converged ($\eta_\infty = 30$) figures used for the Conclusion's Nusselt/Sherwood discussion are given in Table 9.

## Single-Direction Reduction

The $M$-sweep, the domain-independence study and the displacement-thickness calculation below use a single-direction ($x$-only) reduction of the full problem (Eqs. (15)-(16) with $\varphi_2 \equiv 0$), which is also the form used in the Hiemenz/Crane validation of Section 4.2. It serves to establish qualitative trends, and its wall-gradient values are not expected to coincide with the two-directional entries of Table 4 at the same nominal parameters.

## Systematic Variation with $M$

To confirm that the current-aligned/current-reversed differences reported above are systematic rather than an artifact of comparing only $M = \pm 3$, Eq. (15) is solved (momentum equation only, at the single

Table 4 – Variation in $\varphi_{1\eta\eta}(0)$, $-\varphi_{3\eta}(0)$ and $-\varphi_{4\eta}(0)$ with $Fr$, $Da$, $Sc$, $Nb$ and $Nt$, for $M = 3$ (current-aligned case) at the default parameter values stated in Section 4 (full symmetric two-directional model).

| | Blasius | | | Sakiadis | | |
|---|---|---|---|---|---|---|
| Parameters | $\varphi_{1\eta\eta}(0)$ | $-\varphi_{3\eta}(0)$ | $-\varphi_{4\eta}(0)$ | $\varphi_{1\eta\eta}(0)$ | $-\varphi_{3\eta}(0)$ | $-\varphi_{4\eta}(0)$ |
| Fr=0.1 | 0.030995 | 7.150900 | 3.867227 | -0.311941 | 2.333554 | 3.863412 |
| Fr=0.2 | 0.030997 | 7.150902 | 3.867228 | -0.312036 | 2.333342 | 3.863388 |
| Fr=0.3 | 0.031000 | 7.150904 | 3.867229 | -0.312131 | 2.333129 | 3.863365 |
| Da=0.53 | 0.031470 | 7.150982 | 3.867394 | -0.316721 | 2.302628 | 3.861136 |
| Da=0.63 | 0.030997 | 7.150902 | 3.867228 | -0.312036 | 2.333342 | 3.863388 |
| Da=0.73 | 0.030648 | 7.150790 | 3.867101 | -0.308576 | 2.356739 | 3.865089 |
| Sc=1 | 0.030997 | 14.085343 | 1.816387 | -0.312036 | 4.564010 | 1.783543 |
| Sc=2 | 0.030997 | 7.150902 | 3.867228 | -0.312036 | 2.333342 | 3.863388 |
| Sc=3 | 0.030997 | 4.724093 | 5.917716 | -0.312036 | 1.671785 | 5.937590 |
| Nb=0.4 | 0.030997 | 8.843821 | 3.767734 | -0.312036 | 3.705148 | 3.760548 |
| Nb=0.5 | 0.030997 | 7.150902 | 3.867228 | -0.312036 | 2.333342 | 3.863388 |
| Nb=0.6 | 0.030997 | 5.530796 | 3.925924 | -0.312036 | 1.048948 | 3.923895 |
| Nt=0.01 | 0.030997 | 7.676610 | 3.949378 | -0.312036 | 2.409727 | 4.014853 |
| Nt=0.02 | 0.030997 | 7.150902 | 3.867228 | -0.312036 | 2.333342 | 3.863388 |
| Nt=0.03 | 0.030997 | 6.689407 | 3.786471 | -0.312036 | 2.253849 | 3.710388 |

representative parameter set: $\beta = 2$, $Da = 0.63$, $Fr = 0.2$) over $M = -3, -1, 0, 1, 3, 5$ using parameter continuation, for *both* the Blasius configuration ($\lambda_1 = 0$, $\lambda_3 = 1$) and the Sakiadis configuration ($\lambda_1 = 1$, $\lambda_3 = 0$). The sweep covers only the $\varphi_1$ component at this one parameter combination. For $-3 \leq$

Table 5 – Systematic variation of $\varphi_1''(0)$ with $M$, Blasius and Sakiadis configurations (single-direction reduction, $\varphi_2 \equiv 0$; see Section 4.1)

| $M$ | $-3$ | $-1$ | 0 | 1 | 3 | 5 |
|---|---|---|---|---|---|---|
| Blasius, $\varphi_1''(0)$ | 0.5121 | 1.2565 | 1.4977 | 1.7054 | 2.0592 | 2.3606 |
| Sakiadis, $\varphi_1''(0)$ | $-0.0917$ | $-1.0699$ | $-1.3462$ | $-1.5746$ | $-1.9527$ | $-2.2686$ |

$M \leq 5$, $\varphi_1''(0)$ increases monotonically with $M$ in *both* configurations.

## Domain-Independence Study

To justify the far-field boundary $\eta_\infty = 10$ used throughout, Eq. (15) is solved for the representative case $\beta = 2$, $Da = 0.63$, $M = 3$, $Fr = 0.2$, $\lambda_1 = 0$, $\lambda_3 = 1$ over a range of $\eta_\infty$; Table 6 reports the

resulting $\varphi_1''(0)$. The wall gradient $\varphi_1''(0)$ agrees to seven significant digits for all $\eta_\infty \geq 6$, and iden-

Table 6 – Domain-independence check: $\varphi_1''(0)$ versus $\eta_\infty$ (single-direction reduction, $\varphi_2 \equiv 0$; see Section 4.1)

| $\eta_\infty$ | 6 | 8 | 10 | 12 | 15 | 20 |
|---|---|---|---|---|---|---|
| $\varphi_1''(0)$ | 2.0591521 | 2.0591521 | 2.0591521 | 2.0591521 | 2.0591521 | 2.0591521 |

tically (to the $10^{-10}$ solver tolerance) for $\eta_\infty \geq 10$. This confirms that $\eta_\infty = 10$ is sufficient for the momentum field in this representative case.

As a further check, the same representative case ($\beta = 2$, $Da = 0.63$, $M = 3$, $Fr = 0.2$, $\lambda_1 = 0$, $\lambda_3 = 1$, $\eta_\infty = 10$) is solved at successively tighter solver tolerances: $\varphi_1''(0)$ is identical to seven

Table 7 – Solver-tolerance sensitivity: $\varphi_1''(0)$ and achieved maximum residual versus target tolerance (single-direction reduction, $\varphi_2 \equiv 0$; see Section 4.1)

| Target tolerance | $10^{-4}$ | $10^{-6}$ | $10^{-8}$ | $10^{-10}$ |
|---|---|---|---|---|
| $\varphi_1''(0)$ | 2.0591520 | 2.0591521 | 2.0591521 | 2.0591521 |
| Achieved max. residual | $4.3 \times 10^{-5}$ | $6.0 \times 10^{-7}$ | $1.0 \times 10^{-8}$ | $1.0 \times 10^{-10}$ |

significant figures across all four tolerances, confirming that the $10^{-6}$ target tolerance used throughout Sections 3-5 is not a limiting factor for the reported wall-gradient values; the achieved residual tracks the requested tolerance closely (within a factor of $\sim 5$), confirming the solver is not silently under- or over-converging relative to its stated target.

The check is repeated for a current-reversed case, $M = -3$ (other parameters as above, plus $Pr = 6.07$, $Nb = 0.5$, $Nt = 0.02$, $Q^* = 5$, $Sc = 2$, $St = Ss = 3$), reporting $\varphi_1''(0)$, $-\varphi_3'(0)$ and $-\varphi_4'(0)$ together with the maximum boundary-value residual (Eq. (21)). While the momentum wall gradient

Table 8 – Domain-independence check for $M = -3$: momentum, thermal and concentration wall gradients versus $\eta_\infty$ (single-direction reduction, $\varphi_2 \equiv 0$; see Section 4.1)

| $\eta_\infty$ | $\varphi_1''(0)$ | $-\varphi_3'(0)$ | $-\varphi_4'(0)$ | max. residual |
|---|---|---|---|---|
| 10 | 0.51211 | 8.365 | 0.573 | $1.0 \times 10^{-8}$ |
| 15 | 0.51211 | 7.885 | 0.661 | $1.0 \times 10^{-8}$ |
| 20 | 0.51211 | 7.651 | 0.705 | $1.0 \times 10^{-8}$ |
| 30 | 0.51211 | 7.419 | 0.751 | $1.0 \times 10^{-8}$ |
| 40 | 0.51211 | 7.302 | 0.775 | $1.0 \times 10^{-8}$ |

$\varphi_1''(0)$ is domain-independent already at $\eta_\infty = 10$, $-\varphi_3'(0)$ and $-\varphi_4'(0)$ continue to drift noticeably up to $\eta_\infty = 40$ for this strongly heat-generating case ($Q^* = 5$): the thermal and concentration fields decay more slowly than the velocity field and have not fully reached their far-field values at $\eta_\infty = 10$.

All boundary residuals remain at the imposed $10^{-8}$ tolerance throughout, so this drift is a genuine domain-truncation effect rather than a convergence failure. To quantify this across the full Table 4 sweep rather than a single spot check, we recomputed all 15 rows of Table 4 (Blasius, $M = 3$, single-direction proxy) at $\eta_\infty = 30$ and compared to the $\eta_\infty = 10$ values; Table 9 reports the relative changes in $-\varphi_3'(0)$ and $-\varphi_4'(0)$ (the momentum wall gradient $\varphi_1''(0)$ was numerically identical to 5 significant figures at both $\eta_\infty$ for every row, confirming it is robustly domain-independent). Across the sweep,

Table 9 – Relative change (%) in $-\varphi_3'(0)$ and $-\varphi_4'(0)$ from $\eta_\infty = 10$ to $\eta_\infty = 30$, across the full Table 4 parameter sweep (single-direction reduction, $\varphi_2 \equiv 0$; see Section 4.1)

| Row | Value | $\Delta(-\varphi_3'(0))$ | $\Delta(-\varphi_4'(0))$ |
|---|---|---|---|
| $Fr = 0.1, 0.2, 0.3$ | – | $-7.1, -7.0, -7.0$ | $+21.2, +21.2, +21.1$ |
| $Da = 0.53, 0.63, 0.73$ | – | $-7.0, -7.0, -7.1$ | $+21.1, +21.2, +21.2$ |
| $Sc = 1, 2, 3$ | – | $-7.4, -7.0, -6.4$ | $+41.3, +21.2, +15.4$ |
| $Nb = 0.4, 0.5, 0.6$ | – | $-3.6, -7.0, -10.1$ | $+24.0, +21.2, +19.4$ |
| $Nt = 0.01, 0.02, 0.03$ | – | $-4.2, -7.0, -9.5$ | $+17.1, +21.2, +25.3$ |

$-\varphi_3'(0)$ shifts by $-4$ to $-10\%$ and $-\varphi_4'(0)$ by $+15$ to $+41\%$ (the largest shift, $+41\%$, at $Sc = 1$), while the direction of every parameter trend is unchanged between $\eta_\infty = 10$ and 30 in all 15 rows. The domain $\eta_\infty = 10$ is therefore adequate for the momentum-dominated comparisons of this section, whereas quantitative heat- and mass-transfer rates under strong heat generation require $\eta_\infty \geq 30$; the $\eta_\infty = 30$ values are used in the Conclusion.

## Validation Against Limiting-Case and Published Results

To validate the present numerical scheme independently of the full nanofluid/porous/MHD model, the governing equations (15)-(18) are reduced to two classical limiting cases by setting $M = 0$, $Fr = 0$, $Da \to \infty$ ($1/Da = 0$), $\beta \to \infty$ (so $1 + 1/\beta \to 1$), and $\varphi_2 \equiv 0$, so that Eq. (15) reduces to $\varphi_1''' + \varphi_1\varphi_1'' + \lambda_3^2 - \varphi_1'^2 = 0$:

- **Stationary-wall limit (Hiemenz stagnation-point flow)**, $\lambda_1 = 0,\ \lambda_3 = 1$: this is exactly the classical two-dimensional stagnation-point (Hiemenz) flow equation, *not* the classical (zero-pressure-gradient) Blasius equation; the term "Blasius flow" used elsewhere in this manuscript for the stationary-wall configuration follows the stretching-sheet-literature convention (a linear far-field velocity $\propto \lambda_3$), distinct from the original constant-free-stream Blasius problem. The published Hiemenz benchmark is $\varphi_1''(0) = 1.232588$ [9]; the present code, run at this limit, gives $\varphi_1''(0) = 1.232588$, matching to all six reported digits.

- **Moving-wall limit (Crane stretching-sheet flow)**, $\lambda_1 = 1,\ \lambda_3 = 0$: this reduces to the classical Crane stretching-sheet equation $\varphi_1''' + \varphi_1\varphi_1'' - \varphi_1'^2 = 0$, which admits the exact closed-form solution $\varphi_1(\eta) = 1 - e^{-\eta}$, so that $\varphi_1''(0) = -1$ exactly. This is the standard benchmark used to validate the "Sakiadis-type" (moving-wall) configuration in this literature, distinct from Sakiadis's

original constant-wall-velocity problem in an otherwise undisturbed fluid; the present code, run at this limit, gives $\varphi_1''(0) = -1.000008$, within $10^{-5}$ of the exact value.

Both limits are recovered within numerical tolerance without changing the solution algorithm of Section 3.

**Manufactured-solution benchmark (nonzero $Da$, $Fr$, $M$ simultaneously).** The Hiemenz and Crane benchmarks above validate the solver only in the classical $M = 0$, $Fr = 0$, $Da \to \infty$ limit, not the full MHD/porous/Forchheimer model. As an independent check retaining $Da$, $Fr$, and $M$ all simultaneously nonzero, we apply the method of manufactured solutions: choosing the smooth function $\varphi_1(\eta) = \lambda_3\eta - (\lambda_3 - \lambda_1)(1 - e^{-\eta})$, which satisfies the correct boundary conditions ($\varphi_1(0) = 0$, $\varphi_1'(0) = \lambda_1$, $\varphi_1'(\eta_\infty) \to \lambda_3$) but is *not* in general a solution of Eq. (15), we substitute it into Eq. (15) symbolically to compute the residual source term $\mathscr{S}(\eta)$ required to make it an exact solution of the modified equation Eq. (15) $= \mathscr{S}(\eta)$. Adding $\mathscr{S}(\eta)$ to the numerical scheme and re-solving with the same RK45-Newton solver (at $Da = 0.63$, $Fr = 0.2$, $M = 3$, $\beta = 2$, $\lambda_1 = 0$, $\lambda_3 = 1$, $\eta_\infty = 15$) reproduces the manufactured $\varphi_1$, $\varphi_1'$, $\varphi_1''$ to a maximum absolute error of $6 \times 10^{-7}$, $3 \times 10^{-7}$, and $1 \times 10^{-7}$ respectively – consistent with the solver tolerance and confirming that the porous (Darcy), Forchheimer, and MHD terms are implemented correctly in combination, independent of the $M = 0$ Hiemenz/Crane checks above.

**Independent published benchmark: exact MHD-Darcy stretching-sheet solution.** As an additional, independent check against a published result (rather than a self-consistency test), we use the classical exact solution for MHD flow over a linearly stretching sheet with Darcy porous drag, Newtonian fluid, no Forchheimer term: setting $\beta \to \infty$, $Fr = 0$, $\lambda_1 = 1$, $\lambda_3 = 0$ (Sakiadis/Crane configuration) with $M$ and $Da$ both retained nonzero, Eq. (15) reduces to $\varphi_1''' + \varphi_1\varphi_1'' - (1/Da + M)\varphi_1' - \varphi_1'^2 = 0$, $\varphi_1(0) = 0$, $\varphi_1'(0) = 1$, $\varphi_1'(\infty) = 0$, which admits the closed-form exact solution

$$\varphi_1(\eta) = \frac{1 - e^{-\gamma\eta}}{\gamma}, \qquad \gamma = \sqrt{1 + \tfrac{1}{Da} + M},$$

so that $\varphi_1''(0) = -\gamma$; this is the well-known MHD extension (e.g. [25, 33, 34, 27, 28] and references therein) of the original exact Crane solution, generalized here to include the Darcy porous term. At $Da = 0.63$, $M = 3$ (i.e. $\gamma = \sqrt{1 + 1/0.63 + 3} = 2.363747$), the present numerical code gives $\varphi_1''(0) = -2.363747$, matching the exact value to $10^{-13}$ (limited only by solver tolerance). Unlike the Hiemenz/Crane checks, which use $M = 0$, this benchmark independently validates the MHD ($M$) and Darcy ($1/Da$) terms acting together at their default nonzero values; it does not, however, independently validate the Forchheimer, Casson ($\beta < \infty$), or nanofluid/stratification terms, for which no independently published closed-form or benchmark solution combining all of these effects with the present model is known to the authors.

## Relation to Skin Friction, Nusselt, and Sherwood Numbers

The wall gradients $\varphi_1''(0)$, $\varphi_2''(0)$ reported in Table 4 determine the local skin-friction coefficients through the standard definitions $C_{fx} = \tau_{wx}/(\rho_f U_{\text{ref}}^2)$, $C_{fy} = \tau_{wy}/(\rho_f U_{\text{ref}}^2)$ with the reference velocity

$U_{\mathrm{ref}} = ax$ (used instead of the wall velocity, which vanishes in the Blasius-type configuration), with wall shear stresses $\tau_{wx} = \mu_f(1+1/\beta)(v_{1z})_{z=0}$, $\tau_{wy} = \mu_f(1+1/\beta)(v_{2z})_{z=0}$; substituting the similarity transformations of Section 2 gives $C_{fx}Re_x^{1/2} = (1+1/\beta)\varphi_1''(0)$ and $C_{fy}Re_x^{1/2} = (1+1/\beta)\varphi_2''(0)$, with $C_{fy}Re_x^{1/2}$ evaluated along $y = x$ (the symmetric case $\varphi_1 \equiv \varphi_2$ treated here), so that a larger magnitude of $\varphi_1''(0)/\varphi_2''(0)$ corresponds directly to higher wall drag, and its sign indicates the direction of the wall shear relative to the flow. The wall gradients $-\varphi_3'(0)$ and $-\varphi_4'(0)$ reported in Table 4, on which the heat- and mass-transfer statements throughout this section are based, are related to the local Nusselt number $Nu_x$ and local Sherwood number $Sh_x$ through the standard definitions

$$Nu_x = \frac{xh_f}{k_f(\alpha_w - T_0)}, \qquad Sh_x = \frac{xm_f}{B_d(C_w - C_0)}, \tag{22}$$

where $h_f = -k_f(\alpha_z)_{z=0}$ and $m_f = -B_d(C_z)_{z=0}$ are the local wall heat and mass fluxes. The reference differences $\alpha_w - T_0$ and $C_w - C_0$ are the ones used to normalise $\varphi_3$ and $\varphi_4$; Nusselt and Sherwood numbers based on the wall-to-ambient differences $\alpha_w - \alpha_\infty$ and $C_w - C_\infty$ would carry the additional factors $1/(1-St)$ and $1/(1-Ss)$, which are negative for $St, Ss > 1$ because the wall is then colder (and of lower concentration) than the local ambient, so the reference-based definition is used throughout. Substituting the similarity transformations of Section 2 gives the dimensionless forms

$$Nu_x Re_x^{-1/2} = -\varphi_3'(0), \qquad Sh_x Re_x^{-1/2} = -\varphi_4'(0), \qquad Re_x = \frac{ax^2}{\nu_f}, \tag{23}$$

so that an increase in $-\varphi_3'(0)$ corresponds directly to an increase in the dimensionless, Reynolds-number-*scaled* local Nusselt number $Nu_x Re_x^{-1/2}$, and likewise an increase in $-\varphi_4'(0)$ corresponds to an increase in the dimensionless $Sh_x Re_x^{-1/2}$. Statements below about heat- or mass-transfer enhancement refer to these dimensionless, Reynolds-scaled quantities, obtained by varying one dimensionless parameter at fixed $Re_x$; they do not refer to the dimensional coefficients $h_f$ or $m_f$ at fixed physical conditions.

# 5 Entropy Generation Analysis

## Formulation

**General framework: local entropy production as a bilinear flux-force sum.** The local volumetric entropy generation rate for a system with several concurrent irreversible processes follows the standard (Onsager/Clausius-Duhem) result of irreversible thermodynamics: each dissipative mechanism $i$ contributes a term equal to (thermodynamic flux)$_i$×(thermodynamic force)$_i$, divided by the reference temperature,

$$T_\infty S_G''' = \sum_i \mathbf{J}_i \cdot \mathbf{X}_i, \tag{24}$$

where each flux-force pair is non-negative individually for the mechanisms considered here (heat conduction, viscous stress, Joule dissipation, resistive porous drag, and mass diffusion), guaranteeing $S_G''' \geq 0$ term-by-term. Specifically: (a) heat conduction contributes $\mathbf{q} \cdot \nabla(1/T_\infty) = k_f(\nabla T)^2/T_\infty^2$

(Fourier flux times temperature-gradient force); (b) viscous stress contributes $\tau : \nabla \mathbf{v}/T_\infty = \Phi_{visc}/T_\infty$ (stress times strain-rate); (c) Joule dissipation contributes $\mathbf{J} \cdot \mathbf{E}'/T_\infty$ (current times the electric field *in the fluid's own frame*, derived below); (d) *any* resistive body force $\mathbf{F}_{drag}$ opposing relative motion (Darcy *and* Forchheimer porous drag alike) contributes $\mathbf{F}_{drag} \cdot (\mathbf{v} - \mathbf{V})/T_\infty$ – the rate of working of the drag force against the relative flow, converted irreversibly to heat, exactly as for (b) and (c); and (e) mass diffusion contributes the coupled thermal-solutal term via the diffusive flux and its conjugate chemical-potential-gradient force. The same principle is applied below to the Joule, Darcy and Forchheimer terms.

The Joule-heating contribution follows from (c) above: writing $\mathbf{E}' = \mathbf{J}/\sigma_f$ for the electric field in the frame of the moving fluid (as opposed to the externally imposed/reference field $\mathbf{E}$ of Eq. (7), which differs from $\mathbf{E}'$ by the motional term $\mathbf{v} \times \mathbf{B}_0$), the Joule term is $\mathbf{J} \cdot \mathbf{E}'/T_\infty = |\mathbf{J}|^2/(\sigma_f T_\infty)$, manifestly non-negative for *any* current direction, since it depends only on $|\mathbf{J}|^2$ and not on the sign or orientation of $\mathbf{J}$. Using $\mathbf{J} = \sigma_f(\mathbf{v} - \mathbf{V}) \times \mathbf{B}_0$ (Eq. (11)) for the current-aligned case, $|\mathbf{J}|^2 = \sigma_f^2 B_0^2 \big[(v_1 - V_1)^2 + (v_2 - V_2)^2\big]$, so that

$$\frac{\mathbf{J} \cdot \mathbf{E}'}{T_\infty} = \frac{\sigma_f B_0^2}{T_\infty} \big[(v_1 - V_1)^2 + (v_2 - V_2)^2\big]. \tag{25}$$

In the current-reversed configuration, within the signed-Lorentz-force reduced model defined in Section 2 (Eq. (8), $s_M = -1$), the current is taken as $\mathbf{J} \to -\mathbf{J}$ relative to the $M > 0$ reference; this is a property of that reduced model, not a directly derived consequence of reversing $\mathbf{E}$ in the full three-dimensional Ohm's law (which, as shown in Section 2, would instead give a $(\mathbf{v} + \mathbf{V})$-type current). Within the reduced model, the current reverses direction but its magnitude $|\mathbf{J}|$, and hence the dissipation $|\mathbf{J}|^2/\sigma_f$, is unchanged. Consequently the Joule-heating rate (25) is identical for $M > 0$ and $M < 0$, and depends on the model only through the *magnitude* $\sigma_f B_0^2/(\rho_f a) = |M|$, not the signed force-direction parameter $M$ that enters the momentum equations linearly. Hence $|M|$ rather than $M$ appears in the Joule term: in the momentum equations the signed $M$ sets the direction of the Lorentz force, whereas the irreversible Ohmic dissipation depends only on $|\mathbf{J}|^2 \propto |M|$.

The Darcy and Forchheimer porous-drag terms follow from principle (d): both are body forces resisting the relative flow $(v_1 - V_1, v_2 - V_2)$ (as they enter the momentum equations (2)-(3)), and both therefore dissipate energy at the rate (force)$\times$(relative velocity)$/T_\infty$, by the same physical mechanism as any frictional/resistive force – there is no additional postulate specific to either term beyond Eq. (24). For Darcy drag, the force per unit volume is $\mu_f(v_1 - V_1)/K_1$, giving dissipation $\mu_f(v_1 - V_1)^2/(K_1 T_\infty)$ (and analogously in $y$). For Forchheimer drag, the force per unit volume is $\rho_f F_1(v_1^2 - V_1^2) = \rho_f F_1(v_1 - V_1)(v_1 + V_1)$, so the dissipation is $\rho_f F_1(v_1 - V_1)^2(v_1 + V_1)/T_\infty$ (and analogously in $y$); being quadratic in the drag force (itself quadratic in velocity) rather than linear as for Darcy drag, this term is cubic rather than quadratic in the velocity deficit. Both terms dissipate energy only when the local fluid velocity differs from the reference (free-stream or wall) velocity, and correctly vanish when $v_1 \to V_1$, $v_2 \to V_2$, consistent with principle (d).

The full local volumetric entropy generation rate, accounting for thermal, viscous (Casson),

Darcy-porous, Forchheimer-porous, Joule (MHD), and solutal-diffusive irreversibilities, is written as

$$
\begin{aligned}
S_G''' = {} & \frac{k_f}{T_\infty^2}(\alpha_z)^2 + \frac{\mu_f}{T_\infty}\left(1+\frac{1}{\beta}\right)\left[(v_{1z})^2+(v_{2z})^2\right] \\
& + \frac{\sigma_f B_0^2}{T_\infty}\left[(v_1-V_1)^2+(v_2-V_2)^2\right] + \frac{\mu_f}{T_\infty K_1}\left[(v_1-V_1)^2+(v_2-V_2)^2\right] \\
& + \frac{\rho_f}{T_\infty}\Big[F_1(v_1^2-V_1^2)(v_1-V_1)+F_2(v_2^2-V_2^2)(v_2-V_2)\Big] + \frac{RD}{C_\infty}(C_z)^2 + \frac{RD}{T_\infty}\alpha_z C_z .
\end{aligned}
\tag{26}
$$

Using the similarity transformations of Section 2 and the characteristic entropy generation rate $S_0''' = k_f a(\alpha_w-\alpha_\infty)^2/(\nu T_\infty^2)$, the dimensionless *entropy generation number* is obtained as

$$
\begin{aligned}
Ns = {} & \varphi_3'^2 + \frac{Br}{\Omega}\left(1+\frac{1}{\beta}\right)Re\left(\varphi_1''^2+\varphi_2''^2\right) \\
& + \frac{Br}{\Omega}|M|\,Re\left[(\varphi_1'-\lambda_3)^2+(\varphi_2'-\lambda_4)^2\right] + \frac{Br}{\Omega\,Da}Re\left[(\varphi_1'-\lambda_3)^2+(\varphi_2'-\lambda_4)^2\right] \\
& + \frac{Br}{\Omega}FrRe\Big[(\varphi_1'-\lambda_3)^2(\varphi_1'+\lambda_3)+(\varphi_2'-\lambda_4)^2(\varphi_2'+\lambda_4)\Big] \\
& + L\left(\sqrt{\lambda_c}\,\varphi_4' + \frac{\varphi_3'}{2\sqrt{\lambda_c}}\right)^2 ,
\end{aligned}
\tag{27}
$$

where $Br = \mu_f a^2 x^2/[k_f(\alpha_w-\alpha_\infty)]$ is the Brinkman number, $Re = ax^2/\nu$ the local Reynolds number, $\Omega = (\alpha_w-\alpha_\infty)/T_\infty$ the dimensionless temperature-difference (Group) parameter, $L = RD(C_w-C_\infty)/k_f$ the diffusive-constant parameter, and $\lambda_c = (C_w-C_\infty)/(C_\infty\Omega)$ the concentration-ratio parameter.

**Coefficients $L$ and $\lambda_c$.** Substituting $\alpha_z = (\alpha_w-\alpha_\infty)\sqrt{a/\nu}\,\varphi_3'$ and $C_z = (C_w-C_\infty)\sqrt{a/\nu}\,\varphi_4'$ into the diffusive terms of Eq. (26) and dividing by $S_0'''$ gives

$$
\frac{RD}{C_\infty}(C_z)^2/S_0''' = \frac{L\lambda_c}{\Omega}\varphi_4'^2, \qquad \frac{RD}{T_\infty}\alpha_z C_z/S_0''' = \frac{L}{\Omega}\varphi_3'\varphi_4',
\tag{28}
$$

with $L \equiv RD(C_w-C_\infty)/k_f$ and $\lambda_c \equiv (C_w-C_\infty)/(C_\infty\Omega)$. The common factor $1/\Omega$ is absorbed by writing $\widetilde{L} = L/\Omega$ in place of $L$ in Eq. (27). Completing the square in Eq. (27),

$$
\widetilde{L}\left(\sqrt{\lambda_c}\,\varphi_4' + \frac{\varphi_3'}{2\sqrt{\lambda_c}}\right)^2 = \widetilde{L}\lambda_c\varphi_4'^2 + \widetilde{L}\varphi_3'\varphi_4' + \frac{\widetilde{L}}{4\lambda_c}\varphi_3'^2,
\tag{29}
$$

introduces the last term, which has no counterpart in Eq. (26). It is a completion convention, used as in the cited studies, that guarantees $Ns \geq 0$; it slightly overstates the coupled-diffusion contribution. The viscous term uses the velocity gradient $\varphi_1''^2+\varphi_2''^2$, whereas the Joule, Darcy and Forchheimer terms use the velocity deficit $(\varphi_1'-\lambda_3)$, $(\varphi_2'-\lambda_4)$, the Forchheimer term carrying in addition the factor $(\varphi_1'+\lambda_3)$, $(\varphi_2'+\lambda_4)$; all of them vanish as $\eta\to\eta_\infty$, so that $Ns\to 0$ in the far field. The structure

of the Forchheimer term follows from $\rho_f F_1 (v_1 - V_1)^2 (v_1 + V_1)/T_\infty$, and its prefactor $(Br/\Omega)\,Re\,Fr$ is taken by analogy with the Darcy prefactor $Br\,Re/(\Omega\,Da)$, with $Fr$ in the role of $1/Da$, and is adopted as a modelling convention; the bracketed velocity structure follows from direct substitution of $v_1 = ax\varphi_1'$, $V_1 = a\lambda_3 x$ and $F_1 = c_b/(x\sqrt{K_1})$. For the cases computed, $\varphi_1' + \lambda_3 \geq 0$ and $\varphi_2' + \lambda_4 \geq 0$, so the Forchheimer term is non-negative. The absolute value $|M|$ is used in the Joule term because Ohmic dissipation is irreversible and non-negative for either sign of $M$.

Figures 5 and 6, and the $Ns_{\rm tot}/\overline{Be}$ values reported in this section, are computed from the complete expression (27) with the Forchheimer term included, using the full symmetric two-directional model ($\varphi_1 \equiv \varphi_2$, $\lambda_1 = \lambda_2$, $\lambda_3 = \lambda_4$) at the default parameters of Table 2 ($\eta_\infty = 10$; the entropy prefactors are set to $(Br/\Omega)\,Re = 1$, $L = 1$ and $\lambda_c = 1$ in all entropy figures and tables). The Forchheimer share of $Ns_{\rm tot} = \int_0^{\eta_\infty} Ns\,d\eta$ is 0.5% (Blasius, $M = 3$), 0.8% (Blasius, $M = -3$), 0.5% (Sakiadis, $M = 3$) and 1.2% (Sakiadis, $M = -3$): small because, in the full two-directional model, the Forchheimer prefactor $Fr = 0.2$ is compared against *twice* the Joule+Darcy prefactor ($2(|M| + 1/Da)$, from the $\varphi_1 + \varphi_2 = 2\varphi_1$ coupling), which dilutes its relative contribution. The corresponding total entropy values are $Ns_{\rm tot} = 24.1$ ($\overline{Be} = 0.771$) for Blasius $M = 3$, 34.6 ($\overline{Be} = 0.804$) for Blasius $M = -3$, 13.1 ($\overline{Be} = 0.590$) for Sakiadis $M = 3$, and 20.5 ($\overline{Be} = 0.571$) for Sakiadis $M = -3$; the ordering $Ns_{\rm tot}(M{<}0) > Ns_{\rm tot}(M{>}0)$ holds in both flows. The Sakiadis, $M = -3$ case required parameter continuation in $M$ (from $M = 0$) to converge, consistent with the solver sensitivity for strongly current-reversed Sakiadis cases noted in Section 4 (Branch Selection).

**Domain convergence of $Ns_{\rm tot}$.** $Ns_{\rm tot}$ for the default Blasius, $M = 3$ case (single-direction reduction of Section 4.1) was computed at $\eta_\infty = 10, 20, 30, 40, 60, 80, 100$, giving 50.5, 60.3, 66.4, 71.0, 77.6, 82.4, 86.1: the successive 20-unit increments (10.7, 6.6, 4.8, 3.7) shrink, but their ratios (0.62, 0.72, 0.78) increase towards unity rather than settling to a fixed geometric rate, indicating a slowly (rather than exponentially) decaying tail contribution, consistent with $\varphi_3'$, $\varphi_4'$ not reaching their asymptotic far-field decay even at $\eta_\infty = 40$ under this strongly heat-generating ($Q^* = 5$) case. $Ns_{\rm tot}$ is therefore not converged even at $\eta_\infty = 100$. This sequence refers to the single-direction reduction; the totals of Table 10 for the full model (at $\eta_\infty = 10$) are used to compare cases and are not claimed to be domain-converged. By contrast, the corresponding wall gradients at the same $\eta_\infty$ sequence – $-\varphi_3'(0) = 5.404, 5.113, 5.023, 4.982, 4.946, 4.931, 4.924$ and $-\varphi_4'(0) = 0.901, 1.042, 1.092, 1.119, 1.148, 1.164, 1.175$ – *do* converge, essentially stabilizing by $\eta_\infty \approx 60$. This is because $Ns_{\rm tot}$, as a domain integral, accumulates the slowly-decaying far-field tail over an ever-larger interval, whereas the wall gradient depends only on the local near-wall solution; the local wall-gradient quantities reported elsewhere in this paper (Section 4.1) are therefore adequately converged by $\eta_\infty = 40$–$60$ even though $Ns_{\rm tot}$ is not. The corresponding Bejan number, giving the fraction of entropy generation due to heat and mass transfer relative to the total, is

$$Be = \frac{\varphi_3'^2 + L\left(\sqrt{\lambda_c}\varphi_4' + \varphi_3'/2\sqrt{\lambda_c}\right)^2}{Ns}, \qquad 0 \leq Be \leq 1. \tag{30}$$

## Results

Figures 5 present $Ns$ and $Be$ for the Blasius and Sakiadis flows at the baseline parameter set of Table 4 ($St = 3$, $Ss = 3$, $Q^* = 5$, $Sc = 2$, $Pr = 6.07$, $Fr = 0.2$, $Da = 0.63$, $Nb = 0.5$, $Nt = 0.02$), obtained

directly from the solved $\varphi_1, \varphi_2, \varphi_3, \varphi_4$ profiles for $M = \pm 3$.

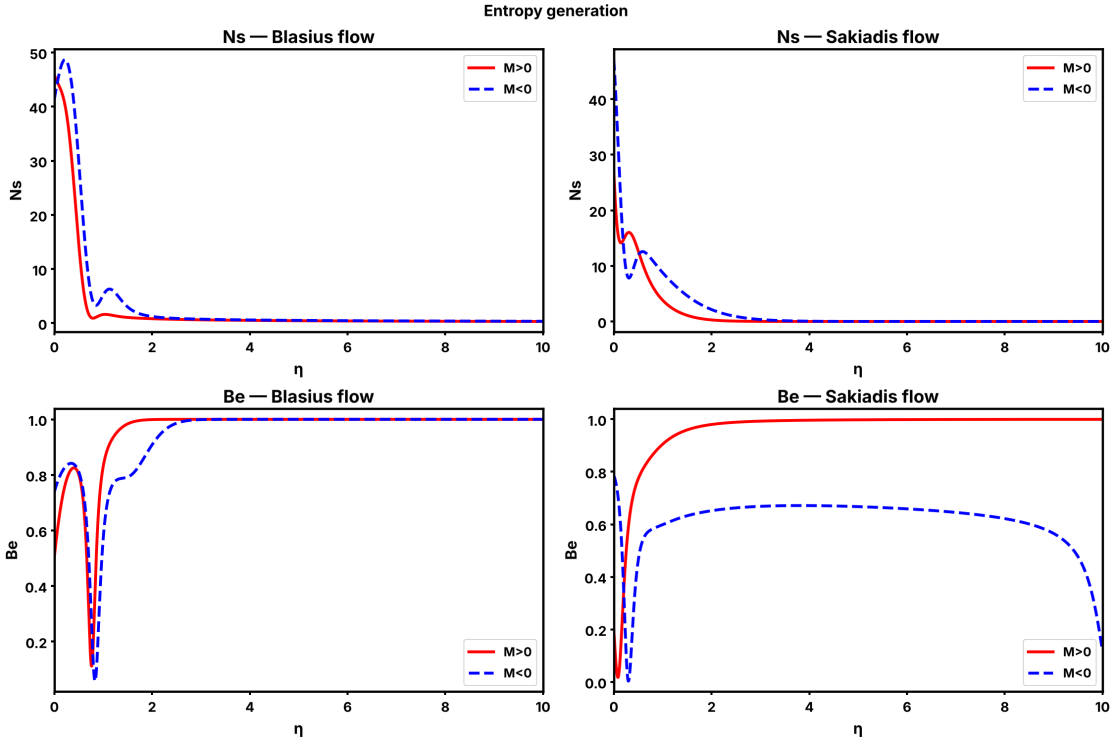



Fig. 5 – Entropy generation number $Ns$ (dimensionless, Eq. (27)) and Bejan number $Be \in [0,1]$ (dimensionless, Eq. (30)) versus the dimensionless similarity coordinate $\eta$, for Blasius and Sakiadis flows, $M > 0$ and $M < 0$, at the parameter values given above.

Near the wall the irreversibility is shared among several mechanisms: for the Blasius flow with $M > 0$ (Fig. 6) the viscous, thermal and mass-diffusion terms are of comparable size at $\eta = 0$, so that $Be$ starts near 0.5, and the thermal contribution peaks at $\eta \approx 0.2$. Away from the wall the thermal and mass-diffusion terms dominate and $Be \to 1$. Integrated over the layer, the current-reversed case generates more entropy than the current-aligned case in both configurations ($Ns_{\mathrm{tot}} = 34.6$ against 24.1 for Blasius and 20.5 against 13.1 for Sakiadis, i.e. increases of 44% and 56%). The pointwise ordering is not uniform. In the Blasius flow, $Ns$ for $M < 0$ is lower at the wall (41.4 against 45.8) but exceeds the $M > 0$ curve for $\eta \gtrsim 0.06$, with a peak of 48.7 at $\eta \approx 0.2$ and a secondary hump near $\eta \approx 1.1$. In the Sakiadis flow, $M < 0$ is higher at the wall (47.1 against 27.0) and for $\eta \gtrsim 0.5$, but lies below the $M > 0$ curve in the band $0.2 \lesssim \eta \lesssim 0.5$, where the $M > 0$ curve has its secondary hump. In the far field $Be \to 1$ for both signs of $M$ in the Blasius flow, whereas for Sakiadis with $M < 0$ it stays near 0.6–0.7 over the layer; close to the outer boundary, where $Ns$ is vanishingly small, $Be$ is sensitive to the boundary condition and drops. Within the parameter range studied, reversing the current therefore increases the total irreversibility in both flows. Fig. 5 shows the total $Ns$ and $Be$ from the full symmetric two-directional model with the complete Forchheimer-inclusive expression

(27); Fig. 6 decomposes $Ns$ into its individual contributions (Blasius, $M = 3$, default parameters, $(Br/\Omega)\,Re = L = \lambda_c = 1$). The near-wall entropy is thus shared between viscous, thermal and mass-

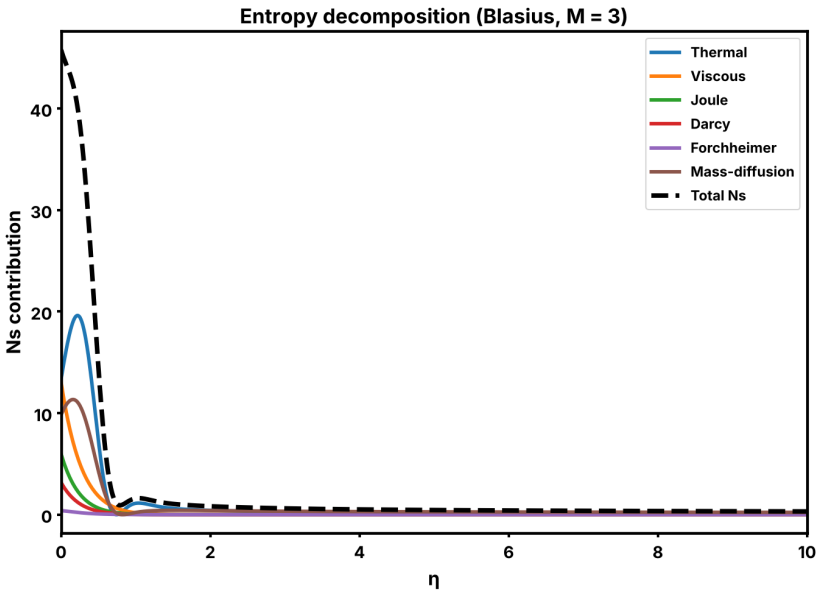



Fig. 6 – Decomposition of the total entropy generation number $Ns$ (Eq. (27)) into thermal, viscous, Joule, Darcy, Forchheimer and mass-diffusion contributions for the Blasius configuration at $M = 3$ (full symmetric two-directional model).

diffusion mechanisms, with Joule and Darcy contributing less and Forchheimer negligibly, whereas the far-field plateau, and hence the rise of $Be$ towards unity, is a thermal/mass-diffusion effect.

Figure 7 shows the effect of the Casson parameter $\beta$ ($\beta = 1, 2, 3, 5$) on $Ns$ and $Be$. In the Blasius flow, increasing $\beta$ lowers the $M < 0$ curve in the near-wall region: its peak falls from 54.0 to 45.5 across $\beta = 1 \to 5$ and the secondary hump near $\eta \approx 1.1$ also decreases, whereas the $M > 0$ curve changes little (wall value $46.3 \to 45.5$). The $M < 0$ curve thus approaches the $M > 0$ curve as $\beta$ increases, and at $\beta = 5$ the two peak values coincide (45.5). In the Sakiadis flow both curves decrease near the wall with increasing $\beta$ ($Ns(0)$ falls from 32.4 to 24.1 for $M > 0$ and from 49.6 to 44.4 for $M < 0$), but the separation between them does not narrow (it grows from 17.2 to 20.3 at the wall). The Bejan number increases with $\beta$ for both signs of $M$: in the Blasius flow the shoulder of the $M < 0$ curve at $1 \lesssim \eta \lesssim 2.5$ shrinks and the curve reaches unity earlier, while in the Sakiadis flow the $M < 0$ value at $\eta = 5$ rises from 0.58 to 0.73 and remains well below the $M > 0$ value ($\approx 1$). Weakening the non-Newtonian effect therefore raises the heat- and mass-transfer share of the irreversibility in all four cases.

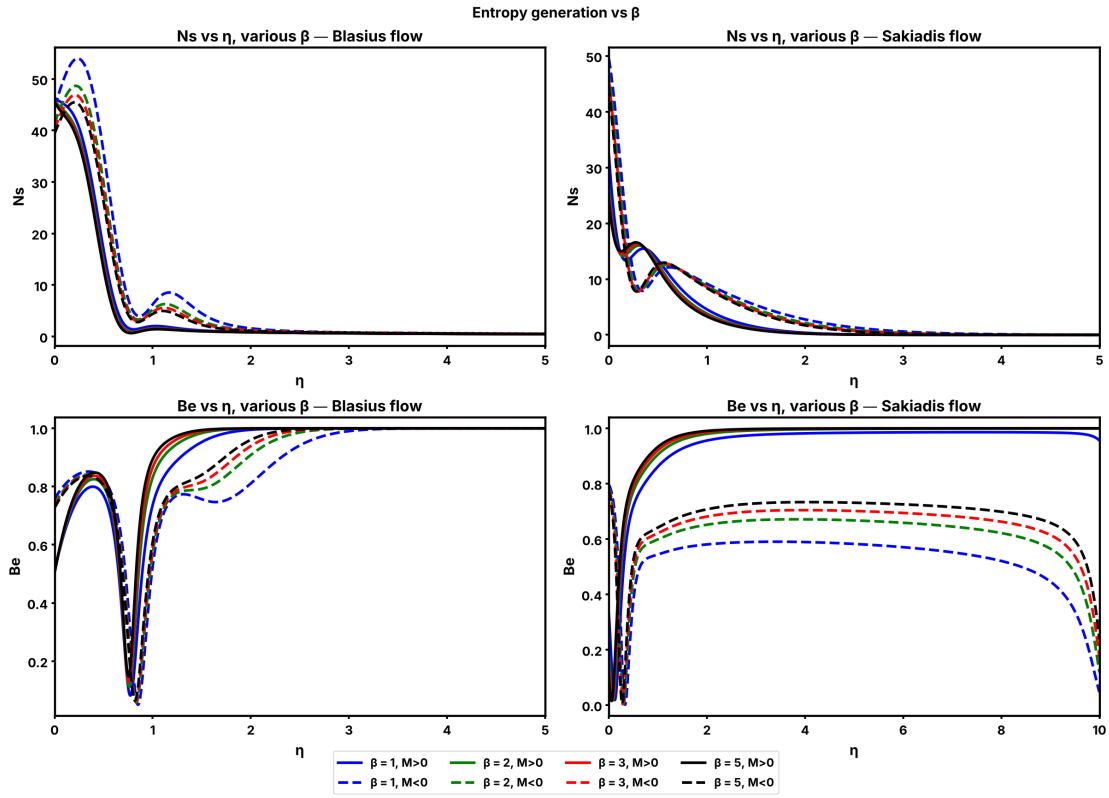



Fig. 7 – Entropy generation number $Ns$ and Bejan number $Be$ (both dimensionless, defined in Eqs. (27)-(30)) versus $\eta$, for $\beta = 1,2,3,5$ in Blasius and Sakiadis flow when $M > 0$ and $M < 0$. Panels (a)–(c) are shown for $0 \leq \eta \leq 5$ for clarity; all computations were performed on $0 \leq \eta \leq 10$.

## Parametric Sensitivity of Entropy Generation

Table 10 reports the domain-integrated entropy generation number, $Ns_{\text{tot}} = \int_0^{\eta_\infty} Ns\, d\eta$, and the entropy-weighted average Bejan number, $\overline{Be} = \int_0^{\eta_\infty} Be\, Ns\, d\eta \,/\, \int_0^{\eta_\infty} Ns\, d\eta$, with $\eta_\infty = 10$ per the domain-independence discussion of Section 4.1 (noting, per that discussion, that a larger $\eta_\infty$ may be needed for full convergence of thermal/concentration-driven quantities under strong heat generation), for the same parameter variations used in Table 4 ($Fr$, $Da$, $Sc$, $Nb$, $Nt$), computed for both $M > 0$ and $M < 0$ in each flow configuration.

All entries are computed from the full symmetric two-directional model; where direct collocation from the default initial guess did not converge, the solution was obtained by continuation in the varied parameter from the baseline solution.

Table 10 shows that $Ns_{\text{tot}}$ decreases with increasing $Nb$ and $Nt$ in all four cases. The response to $Sc$ depends on the configuration: $Ns_{\text{tot}}$ decreases with $Sc$ in the Blasius flow (both signs of $M$) and for Sakiadis with $M < 0$ (where the change between $Sc = 2$ and 3 is negligible), but increases with $Sc$ for Sakiadis with $M > 0$. The Forchheimer parameter has a marked effect only for Blasius with $M < 0$,

Table 10 – Variation of the total entropy generation number $Ns_{\mathrm{tot}}$ and average Bejan number $\overline{Be}$ with $Fr$, $Da$, $Sc$, $Nb$ and $Nt$ (full symmetric two-directional model, $\eta_\infty = 10$).

| | Blasius | | | | Sakiadis | | | |
|---|---|---|---|---|---|---|---|---|
| Parameter | $Ns_{\mathrm{tot}}(M{>}0)$ | $\overline{Be}(M{>}0)$ | $Ns_{\mathrm{tot}}(M{<}0)$ | $\overline{Be}(M{<}0)$ | $Ns_{\mathrm{tot}}(M{>}0)$ | $\overline{Be}(M{>}0)$ | $Ns_{\mathrm{tot}}(M{<}0)$ | $\overline{Be}(M{<}0)$ |
| $Fr = 0.1$ | 24.07 | 0.774 | 36.58 | 0.811 | 13.08 | 0.592 | 20.44 | 0.570 |
| $Fr = 0.2$ | 24.09 | 0.771 | 34.60 | 0.804 | 13.11 | 0.590 | 20.49 | 0.571 |
| $Fr = 0.3$ | 24.12 | 0.768 | 33.15 | 0.799 | 13.14 | 0.588 | 20.56 | 0.573 |
| $Da = 0.53$ | 24.17 | 0.765 | 32.10 | 0.793 | 13.26 | 0.582 | 19.74 | 0.582 |
| $Da = 0.63$ | 24.09 | 0.771 | 34.60 | 0.804 | 13.11 | 0.590 | 20.49 | 0.571 |
| $Da = 0.73$ | 24.04 | 0.775 | 37.80 | 0.815 | 13.00 | 0.596 | 21.04 | 0.562 |
| $Sc = 1$ | 24.52 | 0.775 | 37.58 | 0.820 | 12.80 | 0.580 | 20.64 | 0.574 |
| $Sc = 2$ | 24.09 | 0.771 | 34.60 | 0.804 | 13.11 | 0.590 | 20.49 | 0.571 |
| $Sc = 3$ | 24.09 | 0.771 | 33.38 | 0.797 | 13.34 | 0.597 | 20.48 | 0.571 |
| $Nb = 0.4$ | 25.19 | 0.781 | 37.33 | 0.819 | 13.57 | 0.604 | 21.19 | 0.586 |
| $Nb = 0.5$ | 24.09 | 0.771 | 34.60 | 0.804 | 13.11 | 0.590 | 20.49 | 0.571 |
| $Nb = 0.6$ | 23.16 | 0.762 | 32.30 | 0.790 | 12.84 | 0.581 | 19.85 | 0.557 |
| $Nt = 0.01$ | 24.45 | 0.774 | 35.61 | 0.810 | 13.18 | 0.592 | 20.67 | 0.575 |
| $Nt = 0.02$ | 24.09 | 0.771 | 34.60 | 0.804 | 13.11 | 0.590 | 20.49 | 0.571 |
| $Nt = 0.03$ | 23.75 | 0.767 | 33.66 | 0.799 | 13.04 | 0.588 | 20.32 | 0.568 |

where $Ns_{\mathrm{tot}}$ decreases from 36.6 to 33.2 as $Fr$ increases from 0.1 to 0.3; in the other three cases it changes $Ns_{\mathrm{tot}}$ by less than 0.5%. The response to $Da$ depends on the sign of $M$: $Ns_{\mathrm{tot}}$ decreases with $Da$ for $M > 0$ in both flows, but increases with $Da$ for $M < 0$ in both flows. Because the Joule and Darcy terms in Eq. (27) are written in terms of the velocity *deficit* $(\varphi_1' - \lambda_3, \varphi_2' - \lambda_4)$ relative to the reference flow rather than the absolute velocity, the current-reversed regime generates higher total entropy than the current-aligned regime in both configurations, i.e. $Ns_{\mathrm{tot}}(M{<}0) > Ns_{\mathrm{tot}}(M{>}0)$ for every entry of Table 10.

# Conclusion

This study compared Blasius-type and Sakiadis-type flows of a Casson nanofluid under thermal and solutal stratification, using the signed-Lorentz-force reduced model of Section 2, in which $M > 0$ follows from the quasi-static Lorentz force and $M < 0$ is a postulated sign-reversed force. The main findings are as follows.

- **Flow behaviour:** The velocity responds to $\beta$ in opposite ways for $M > 0$ and $M < 0$ (Figs. 2a–2b). For $M < 0$ the Blasius-type flow develops reverse flow near the wall, whereas the Sakiadis-type flow is accelerated above its wall velocity.
- **Stratification:** Increasing $St$ and $Ss$ lowers the wall values $\varphi_3(0) = 1 - St$ and $\varphi_4(0) = 1 - Ss$ and, for $M < 0$, produces a negative undershoot of temperature and concentration. In Blasius-

type flow with $M > 0$ the temperature has a pronounced maximum near the wall that grows with $St$.

- **Heat and mass transfer:** With $Nu_x Re_x^{-1/2} = -\varphi_3'(0)$ and $Sh_x Re_x^{-1/2} = -\varphi_4'(0)$ (Section 4.2), the $\eta_\infty = 30$ values of Table 9 (Blasius case) show that $Nu_x Re_x^{-1/2}$ decreases by about 18% as $Nt$ increases from 0.01 to 0.03, by 34% as $Nb$ increases from 0.4 to 0.6 and by 36% as $Sc$ increases from 1 to 3, while $Sh_x Re_x^{-1/2}$ increases by about 84% with $Sc$ and 7% with $Nb$. The effect of $Nt$ on $Sh_x Re_x^{-1/2}$ is below 1% and changes sign between $\eta_\infty = 10$ and 30. These percentages refer to the single-direction reduction of Section 4.1.

- **Boundary-layer thinning and wall drag:** The displacement thickness $\delta^*$ decreases monotonically with $\beta$ for Blasius-type flow (both signs of $M$) and Sakiadis-type flow with $M > 0$.

- **Entropy generation:** Integrated over the boundary layer, the current-reversed case ($M < 0$) generates more entropy than the current-aligned case ($M > 0$) in both configurations, by 44% in the Blasius-type flow and 56% in the Sakiadis-type flow at the default parameters. The pointwise ordering is not uniform near the wall.

The configurations studied are idealized, and applications such as MHD flow control, thermal management and nanofluid heat exchangers are motivations rather than results of this work.

## Limitations

The electromagnetic formulation uses the quasi-static (low-magnetic-Reynolds-number) approximation with a uniform applied field, and $M < 0$ is a postulated signed force rather than a solution of the full vector Ohm's law under field reversal. The similarity reduction of the energy and concentration equations (17)-(18) follows the convention of the cited stratified-stretching-sheet literature [25, 33, 34, 27, 28]; a literal substitution of Eqs. (4)-(5) reproduces the diffusive and momentum-coupling terms exactly but gives the heat-generation and stratification-coupling coefficients differing by factors of $Pr$ and 2, respectively. The mass-diffusion entropy term is an ideal-gas-based convention applied to a liquid suspension, and the entropy totals are not domain-converged. The supplementary checks of Section 4.1 use the single-direction reduction, the parameter range is limited (Table 2), and no stability or bifurcation analysis of possible competing solution branches has been carried out. The validation of Section 4.2 recovers the Hiemenz and Crane solutions, an exact MHD–Darcy solution and a manufactured solution of the momentum equation; no experimental comparison or benchmark for the complete model is available.

Future work could include experimental validation, a stability analysis of the solution branches, and extensions to more complex geometries.

# References

[1] Sakiadis B. C., Boundary-layer behavior on continuous solid surfaces: I. Boundary-layer equations for two-dimensional and axisymmetric flow, AIChE, 1961, 7(1), 26-28.

[2] Crane L. J., Flow past a stretching plate, Zeitschrift für angewandte Mathematik und Physik ZAMP, 1970, 21(4), 645-647.

[3] Liu I. C., Andersson H. I., Heat transfer over a bidirectional stretching sheet with variable thermal conditions, International Journal of Heat and Mass Transfer, 2008, 51(15-16), 4018-4024.

[4] Nadeem S., Haq R. U., Khan Z. H., Numerical study of MHD boundary layer flow of a Maxwell fluid past a stretching sheet in the presence of nanoparticles, Journal of the Taiwan Institute of Chemical Engineers, 2014, 45(1), 121-126.

[5] Rajagopal K. R., Na T. Y., Gupta A. S., Flow of a viscoelastic fluid over a stretching sheet, Rheologica Acta, 1984, 23(2), 213-215.

[6] Ganguly S., et al., Electrokinetic effects in nanofluids, Journal of Nanoparticle Research, 2014, 16(1), 1-15.

[7] Sheikholeslami M., New computational approach for MHD nanofluid, Computer Methods in Applied Mechanics and Engineering, 2019, 344, 306-318.

[8] Ellahi R., et al., Non-Newtonian nanofluids in industrial processes, Journal of Molecular Liquids, 2015, 211, 544-550.

[9] Schlichting H., Gersten K., Boundary-Layer Theory, Springer, 2016.

[10] Choi S. U. S., et al., Nanofluids for thermal management, Advanced Materials, 2009, 21(10), 1044-1048.

[11] Squires T. M., Quake S. R., Microfluidics: Fluid physics at the nanoliter scale, Reviews of Modern Physics, 2005, 77(3), 977-1026.

[12] Tripathi D., et al., Casson nanofluid flow in microvascular systems, Journal of Biomechanics, 2021, 120, 110345.

[13] Adrian R. J., Westerweel J., Particle Image Velocimetry, Cambridge University Press, 2011.

[14] White F. M., Viscous Fluid Flow, McGraw-Hill, 2006.

[15] Buongiorno J., Convective transport in nanofluids, ASME Journal of Heat Transfer, 2006, 128(3), 240-250.

[16] Blasius H., Grenzschichten in Flüssigkeiten mit kleiner Reibung, Zeitschrift für Mathematik und Physik, 1908, 56, 1-37.

[17] Prandtl L., Über Flüssigkeitsbewegung bei sehr kleiner Reibung, Verhandlungen des III. Internationalen Mathematiker-Kongresses, Heidelberg, 1904, 484-491 (English translation: Motion of fluids with very little viscosity, NACA Technical Memorandum 452, 1928).

[18] Ridha A., On the three-dimensional alternative to the Blasius boundary-layer solution, Comptes Rendus Mecanique, 2005, 333(10), 768-772.

[19] Kachanov Y. S., A. Michalke, Three-dimensional instability of the Blasius boundary layer, In Laminar-turbulent transition, Springer, Berlin, Heidelberg, 1995, 473-480.

[20] Tsigklifis K., Lucey A. D., Global stability of three-dimensional disturbances in Blasius boundary-layer flow over a compliant panel, In 19th Australian Fluid Mechanics Conference, Melbourne, Australia, 2014.

[21] Kumar R., Kumar R., Shehzad S. A., Chamkha A. J., Optimal treatment of stratified Carreau and Casson nanofluids flows in Darcy-Forchheimer porous space over porous matrix, Applied Mathematics and Mechanics,2020, 41, 1651-1670.

[22] Razavi S. M., Azhdari S., Taheri-Behrooz F., Effect of the crude oil environment on the electrical conductivity of the epoxy nanocomposites, Advances in Nano Research, 2023, 15(4) 285-294.

[23] Chandrasekhar S., Woltjer L., On force-free magnetic fields. National Academy of Sciences, 1958, 44 (4) 285-289.

[24] Ledvina S. A., Cravens T. E., A three-dimensional MHD model of plasma flow around Titan. Planetary and Space Science, 1998, 46(9-10), 1175-1191.

[25] Kumar R., Kumar R., Koundal R., Shehzad S. A., Sheikholeslami M., Cubic auto-catalysis reactions in three-dimensional nanofluid flow considering viscous and Joule dissipations under the thermal jump. Communications in Theoretical Physics, 2019, 71(7) 779.

[26] Hawley J. F., Balbus, S. A., Stone J. M., A magnetohydrodynamic nonradiative accretion flow in three dimensions. The Astrophysical Journal Letters, 2001, 554(1), L49.

[27] Kumar R., Sharma T., Kumar R., Sheikholeslami M., Vajravelu K., Stability analysis of multiple solutions in case of a stretched nanofluid flow obeying Corcione's correlation: An extended Darcy model. ZAMM-Journal of Applied Mathematics and Mechanics/Zeitschrift für Angewandte Mathematik und Mechanik, 2021, 101(5), e202000172.

[28] Pantokratoras A., Non-similar Blasius and Sakiadis flow of a non-Newtonian Carreau fluid, Journal of the Taiwan Institute of Chemical Engineers, 2015, 56 1-5.

[29] Hayat T., Qasim, M., Abbas Z., Homotopy solution for the unsteady three-dimensional MHD flow and mass transfer in a porous space. Communications in Nonlinear Science and Numerical Simulation, 2010, 15(9), 2375-2387.

[30] Chand K., Kumar R., Hall effect on heat and mass transfer in the flow of oscillating viscoelastic fluid through porous medium with wall slip conditions. Indian Journal of Pure & Applied Physics, 2012, 50, 149-155.

[31] Kumar R., Kumar R., Shehzad S. A., Three-dimensional upper-convected Maxwell nanofluid transport due to cross-diffusion and stratification: Numerical solutions, Numerical Heat Transfer, Part B: Fundamentals, 2023, 84(6), 1-16.

[32] Othma Mohamed I. A., Samia M. S. and Elsayed M. Abd-Elaziz, Effect of magnetic field and gravity on thermoelastic fiber-reinforced with memory-dependent derivative, Advances in Materials Research, 2023, 12(2), 101-118.

[33] Mustafa M., Khan J. A., Hayat T., Alsaedi A., Sakiadis flow of Maxwell fluid considering the magnetic field and convective boundary conditions, AIP Advances, 2015, 5(2), 027106.

[34] Xiangyang L., Xu J., Lai T., He M., Investigation on the heat transfer of MHD nanofluids in channel containing porous medium using lattice Boltzmann method, Advances in Nano Research, 2023, 15(3), 191-201.

[35] Hayat T., Aziz A., Muhammad T., Alsaedi A., Darcy–Forchheimer three-dimensional flow of Williamson nanofluid over a convectively heated nonlinear stretching surface, Communications in Theoretical Physics, 2017, 68(3), 387.

[36] Muhammad T., Alsaedi A., Hayat A., Shehzad S. A., A revised model for Darcy-Forchheimer three-dimensional flow of nanofluid subject to convective boundary condition, Results in Physics, 2017, 7, 2791-2797.

[37] Hayat T., Haider F., Muhammad T., Alsaedi A., Three-dimensional rotating flow of carbon nanotubes with Darcy-Forchheimer porous medium PloS one, 2017, 12(7), e0179576.

[38] Vafai K., Porous media: Applications in biological systems and biotechnology. CRC Press, Boca Raton, 2010.

[39] Vafai K., Tien C. L., Boundary and inertia effects on flow and heat transfer in porous media. International Journal of Heat and Mass Transfer, 1981, 24(2), 195-203.

[40] Vafai K., Tien C.L., Boundary and inertia effects on convective mass transfer in porous media. International Journal of Heat and Mass Transfer, 1982, 25(8), 1183-1190.

[41] Nield D. A., The limitations of the Brinkman-Forchheimer equation in modeling flow in a saturated porous medium and at an interface. International Journal of Heat and Fluid Flow, 1991, 12(3), 269-272.

[42] Eckert E. R. G., Drake Jr. R. M., Analysis of heat and mass transfer, NY (USA), 1997, 19(23).

[43] Ganesan P., Suganthi R. K., Loganathan P., Soret and Dufour effects in a free convective doubly stratified flow over a vertical plate with chemical reaction, Chemical Engineering Communications, 2013, 200(4), 514-531.